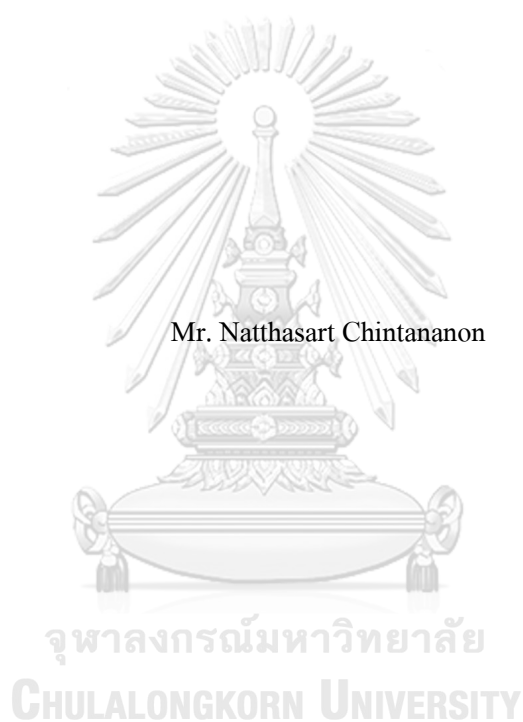


EFFECTS OF MAGNESIUM SUBSTITUTION ON ELECTRONIC PROPERTIES OF
CALCIUM DIFLUORIDE



A Thesis Submitted in Partial Fulfillment of the Requirements

for the Degree of Master of Science in Physics

Department of Physics

FACULTY OF SCIENCE

Chulalongkorn University

Academic Year 2019

Copyright of Chulalongkorn University

ผลของการแทนที่ของแมกนีเซียมต่อสมบัติทางอิเล็กทรอนิกส์ของแคลเซียมไดฟลูออไรด์



วิทยานิพนธ์นี้เป็นส่วนหนึ่งของการศึกษาตามหลักสูตรปริญญาวิทยาศาสตรมหาบัณฑิต

สาขาวิชาฟิสิกส์ ภาควิชาฟิสิกส์

คณะวิทยาศาสตร์ จุฬาลงกรณ์มหาวิทยาลัย

ปีการศึกษา 2562

ลิขสิทธิ์ของจุฬาลงกรณ์มหาวิทยาลัย

Thesis Title EFFECTS OF MAGNESIUM SUBSTITUTION ON
 ELECTRONIC PROPERTIES OF CALCIUM DIFLUORIDE
By Mr. Natthasart Chintananon
Field of Study Physics
Thesis Advisor Associate Professor UDOMSILP PINSOOK, Ph.D.
Thesis Co Advisor Prutthipong Tsuppayakorn-aek, Ph.D.

Accepted by the FACULTY OF SCIENCE, Chulalongkorn University in Partial
Fulfillment of the Requirement for the Master of Science

..... Dean of the FACULTY OF SCIENCE
(Professor POLKIT SANGVANICH, Ph.D.)

THESIS COMMITTEE

..... Chairman
(Associate Professor SAKUNTAM SANORPIM, Ph.D.)

..... Thesis Advisor
(Associate Professor UDOMSILP PINSOOK, Ph.D.)

..... Thesis Co-Advisor
(Prutthipong Tsuppayakorn-aek, Ph.D.)

..... Examiner
(Associate Professor SURACHATE LIMKUMNERD, Ph.D.)

..... External Examiner
(Associate Professor Prayoonsak Pluengphon, Ph.D.)

ณัฐศาสตร์ จินตนา นนท์ : ผลของการแทนที่ของแมกนีเซียมต่อสมบัติทาง
อิเล็กทรอนิกส์ของแคลเซียมไดฟลูออไรด์. (EFFECTS OF MAGNESIUM
SUBSTITUTION ON ELECTRONIC PROPERTIES OF
CALCIUM DIFLUORIDE) อ.ที่ปรึกษาหลัก : รศ. ดร.อุดมศิลป์ ปิ่นสุข, อ.ที่ปรึกษา
ร่วม : ดร.พฤทธิพงษ์ ทรัพย์กรเอก

ทฤษฎีฟังก์ชันนอลความหนาแน่นถูกใช้เพื่อคำนวณหาการเปลี่ยนโครงสร้างของ
แคลเซียมไดฟลูออไรด์ จากผลการคำนวณพบว่าแคลเซียมไดฟลูออไรด์มีโครงสร้างเป็น Fm-
3m ในช่วงความดัน 0-8 GPa และมีโครงสร้างเป็น Pnma ตั้งแต่ความดัน 8 GPa เป็นต้นไป จาก
การคำนวณหาโครงสร้างแถบพลังงานพบว่าแคลเซียมไดฟลูออไรด์มีคุณสมบัติทางไฟฟ้าเป็นฉนวน
นอกจากนี้ยังพบว่าแถบพลังงานของแคลเซียมไดฟลูออไรด์มีค่าเพิ่มขึ้นตามความดันตั้งแต่ 0 ถึง 70
GPa จากนั้นลดลงอย่างกะทันหันที่ความดัน 70 GPa ในงานวิจัยนี้ศึกษา เราได้เจือแมกนีเซียมสู่
โครงสร้างของแคลเซียมไดฟลูออไรด์โดยใช้คลัสเตอร์เอ็กซ์แพนชันพบว่า $Mg_{0.25}Ca_{0.75}F_2$ มี
โครงสร้าง Pm ซึ่งมีความเสถียรที่ความดัน 70 GPa และสรุปได้ว่าการเจือแมกนีเซียมสู่โครงสร้าง
ของแคลเซียมไดฟลูออไรด์ช่วยให้แถบพลังงานของ $Mg_{0.25}Ca_{0.75}F_2$ สูงขึ้นตั้งแต่ความดัน 70
GPa เป็นต้นไป

จุฬาลงกรณ์มหาวิทยาลัย
CHULALONGKORN UNIVERSITY

สาขาวิชา ฟิสิกส์
ปีการศึกษา 2562

ลายมือชื่อนิสิต

ลายมือชื่อ อ.ที่ปรึกษาหลัก

ลายมือชื่อ อ.ที่ปรึกษาร่วม

6172129023 : MAJOR PHYSICS

KEYWORD: DFT, high pressure, calcium difluoride, magnesium difluoride, cluster expansion, phase transition

Natthasart Chintananon : EFFECTS OF MAGNESIUM SUBSTITUTION ON ELECTRONIC PROPERTIES OF CALCIUM DIFLUORIDE. Advisor: Assoc. Prof. UDOMSILP PINSOOK, Ph.D. Co-advisor: Prutthipong Tsuppayakorn-aek, Ph.D.

We use density functional theory to find the phase transitions of CaF_2 . The results show that CaF_2 adopts the fluorite structure, with the space group Fm-3m, in the range of 0-8 GPa and transforms into the cotunnite structure, with the space group Pnma, above 8 GPa. The electronic band structure of the Pnma- CaF_2 structure expresses an insulating phase, and the bandgap collapses under pressure above 70 GPa. In this work, we proposed a new decoration of Ca/Mg-substituted fluorides $\text{Mg}_x\text{Ca}_{1-x}\text{F}_2$, using the cluster expansion technique which is commonly used to study alloys. We found that the $\text{Mg}_{0.25}\text{Ca}_{0.75}\text{F}_2$, with a Pm structure, is stable at 70 GPa. Our electronic band structure calculations indicate that the substitution of Mg increases the bandgaps of the $\text{Mg}_{0.25}\text{Ca}_{0.75}\text{F}_2$ compounds above 70 GPa.

จุฬาลงกรณ์มหาวิทยาลัย
CHULALONGKORN UNIVERSITY

Field of Study: Physics

Academic Year: 2019

Student's Signature

Advisor's Signature

Co-advisor's Signature

ACKNOWLEDGEMENTS

I sincerely appreciate my thesis advisor Assoc. Prof. Dr. Udomsilp Pinsook for letting me in Extreme Condition Research Laboratory and giving me invaluable advice. I would like to thank my co-advisor Dr. Prutthipong Tsuppayakorn-aeek, and Wiwittawin Sukmas for teaching me how to use all of the computational programs. Without them, this work won't be accomplished. I would like to thank everyone in Extreme Condition Research Laboratory for giving me warm welcome, staying with me when I am weary, and lending me their strength. This place is not only a workplace but rather a home. Furthermore, I wish to thank Assoc. Prof. Dr. Prayoonsak Pluengphon, Assoc. Prof. Dr. Sakuntam Sanorpim, and Assoc. Prof. Dr. Surachate Limkumnerd for being my thesis's committee and giving useful comments on my thesis. Finally, I would like to thank my mom and my friends at Photisarn Pittayakorn School, Chulalongkorn University.

Natthasart Chintananon

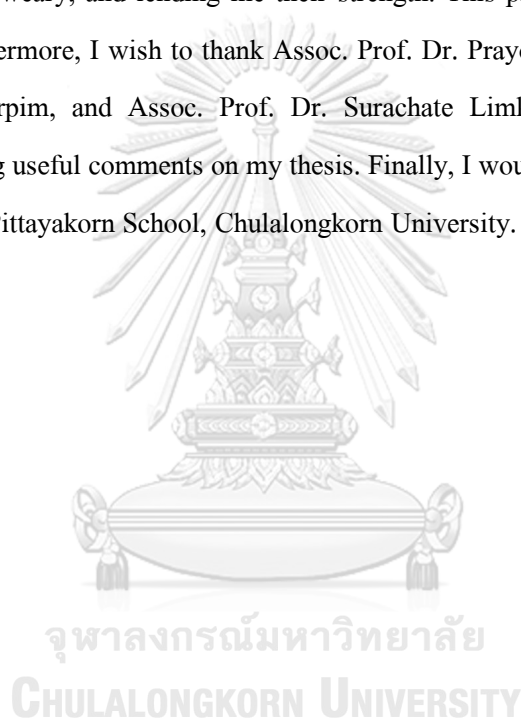


TABLE OF CONTENTS

	Page
ABSTRACT (THAI)	iii
ABSTRACT (ENGLISH).....	iv
ACKNOWLEDGEMENTS.....	v
TABLE OF CONTENTS	vi
1.INTRODUCTION	1
2. THEORETICAL BACKGROUND	6
2.1 Density functional theory.....	8
2.1.1 Hohenberg-Kohn existence theorem.....	8
2.1.2 Hohenberg-Kohn variational theorem.....	9
2.2 The Kohn-Sham Energy	9
2.3 The exchange-correlation functional	11
2.3.1 Local Density Approximation (LDA).....	11
2.3.2 Generalised Gradient Approximation (GGA).....	11
2.4 The Kohn-Sham Equation	12
2.5 The secular equation	14
2.6 Techniques of DFT calculation	15
2.6.1 Plane wave basis set	15
2.6.2 Pseudopotentials and Projection augmented Wave	16
2.6.3 The Ultrasoft pseudopotential	20
2.6.4 Cutoff energy and k-point mesh.....	22
2.6.5 Geometry optimization.....	22

2.6.6 Cluster expansion	24
2.6.7 Phase transitions	25
2.6.8 Gibbs free energy.....	26
2.6.9 Phonon dispersion relation	27
2.6.10 Band structure.....	28
2.6.11 Density of states.....	30
3.CALCULATION DETAILS	31
3.1 Convergence test of CaF ₂	32
3.2 Relaxed structures of CaF ₂ and MgF ₂	33
4.RESULTS AND DISCUSSIONS	35
4.1 Phase transitions confirmation.....	35
4.1.1 Phase confirmation of CaF ₂	35
4.1.2 Phase confirmation of MgF ₂	37
4.2 Plotting of bandgap of CaF ₂ versus pressure	38
4.3 Determining the lowest formation energy of Mg _x Ca _{1-x} F ₂ at 70 GPa	39
4.3.1 Electronic band structures of Mg _x Ca _{1-x} F ₂ , MgF ₂ and CaF ₂ at 70 GPa	41
4.3.2 Projected density of states of Mg _x Ca _{1-x} F ₂ , MgF ₂ and CaF ₂	44
5. CONCLUSION	47
REFERENCES	48
VITA	53

1.INTRODUCTION

Nowadays, electronic waste is one of the most serious problem that we need to pay serious attention. As shown in Figure 1.1, the total electronic waste constantly rises worldwide every year and is predicted to be 55.2 million metric tonnes in 2021. Most of 44.7 million metric tonnes, in 2016, were embedded in landfill and were incinerated. Therefore, the by-product can cause leachate and air pollution, respectively.

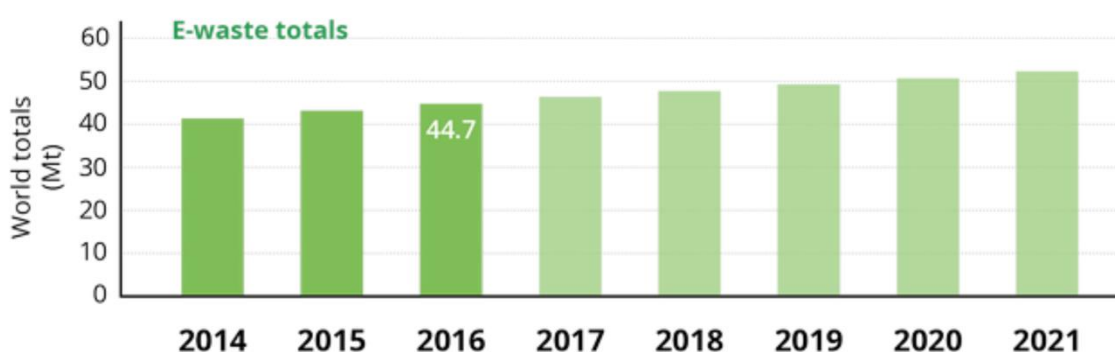


Figure 1.1: Bar graph for electronic waste (million tonnes) from 2014 to 2021

(<https://www.itu.int/en/ITU-D/Environment/Pages/Toolbox/Global-E-waste-Monitor-2017.aspx>)

To reduce the electronic waste produced each year, the electronic devices should be made from environmental friendly element. Several studies have shown that Ca/Mg-binary alloy improves electronic and physical properties of Mg-anode and is biodegradable material [1-4]. In 2018, Deng M., *et al.* have shown that Ca enhances the discharge voltage of Mg-anode and reduces the self-corrosion of Mg-anode [5]. Moreover, volumetric capacity of Mg rechargeable battery is comparable with Li rechargeable battery [6]. For all the reasons mentioned above, we are interested in Ca/Mg-binary alloy. We used CaF_2 and MgF_2 as inputs for our theoretical calculations.

CaF_2 adopts face center cubic, $\text{Fm}\bar{3}\text{m}$, at the ambient condition. Cui S., *et al.* showed that the pressure induced phases of CaF_2 are in the following order [7]: $\text{Fm}\bar{3}\text{m} \rightarrow \text{Pnma}$ (8.1GPa) $\rightarrow \text{P63/mmc}$ (278GPa). As depicted in Figure 1.2, Nelson J R., *et al.* calculated the enthalpy in the pressure range of 0-70 GPa and found that the phases transformation of CaF_2 are in the following

order [8]: $Fm\bar{3}m \rightarrow Pnma$ (8.1GPa). The picture of unit cell of each phase is depicted in Figure 1.3. The phase transitions have been experimentally confirmed by X-ray diffraction [9]. CaF_2 has many interesting applications in wide area of physics and chemistry. It can be used in glass manufacturing because it has very high transmittance [10]. It can be used as an oxygen-free substrate for FeSe thin film since the oxygen-based substrate leads to low quality FeSe thin film. Moreover, it enhances superconducting transition temperature (T_c) of FeSe thin film [11]. In diamond anvil cell, it can be used as an internal pressure calibrator because it endures wide range of temperature and pressure and it won't impede the x-ray diffraction during the structure searching process [12]. The previous studies have revealed that the band gap of CaF_2 increases with increasing pressure ranging from 0-70 GPa so the two high pressure phases, Pnma and P63/mmc, are insulators. Above 70 GPa, the gap begins to collapse, see Figure 1.4 [13]. Many groups of researchers further reduce the gap by doping impurities, such as Pr^{3+} [14, 15], Nd^{3+} [16, 17] and Yb [18], to the CaF_2 . But we interested in enhancing the gap by doping Mg to the CaF_2 system at 70 GPa.

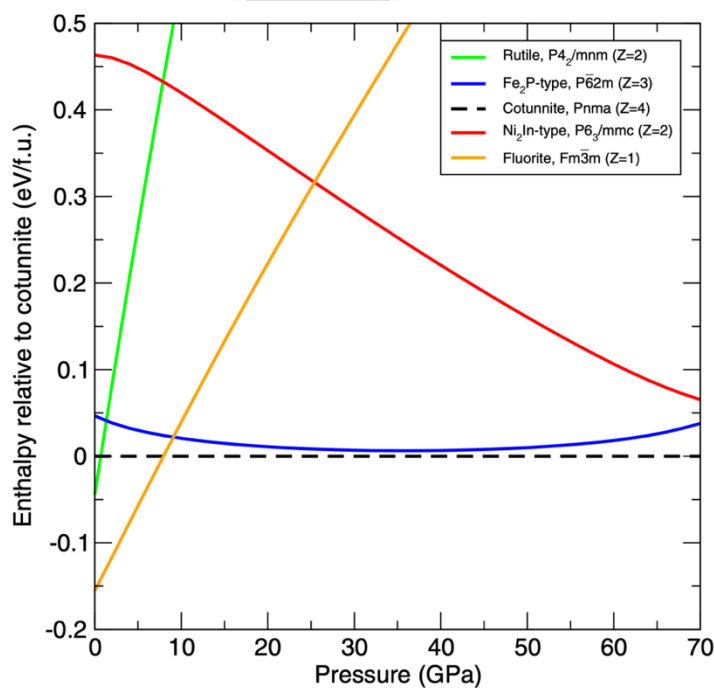


Figure 1.2: The enthalpy of CaF_2 relative to cotunnite versus pressure [8]

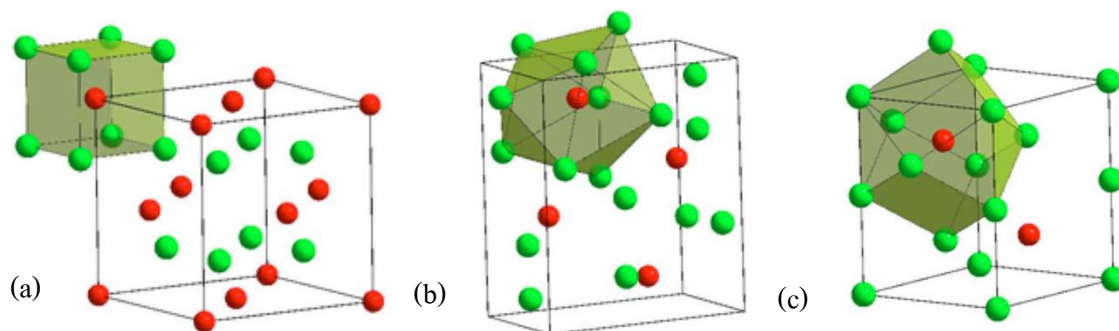


Figure 1.3: The unit cell of CaF_2 , (a) $Fm\bar{3}m$ (b) $Pnma$ (c) $P6_3/mmc$ [13]

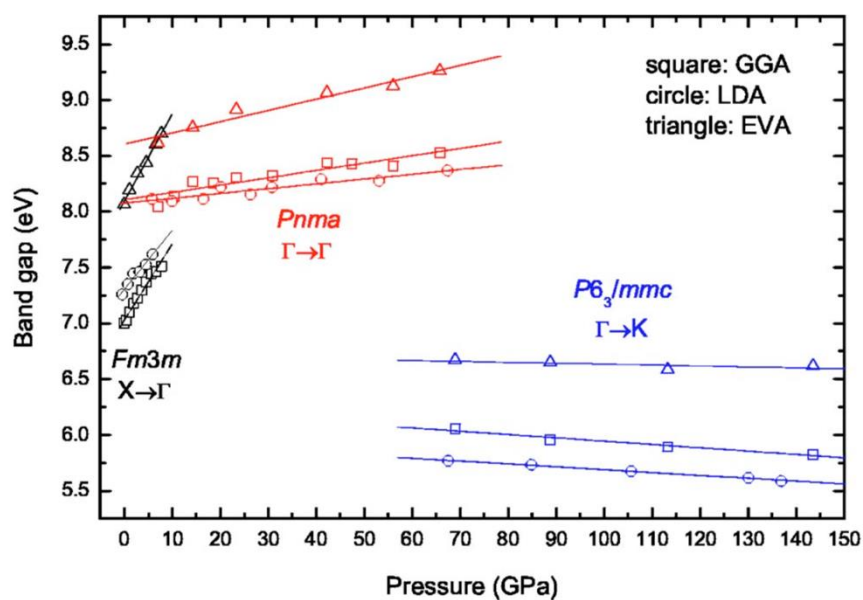


Figure 1.4: The band gap of CaF_2 against pressure. The band gap of $Fm\bar{3}m$, $Pnma$ and $P6_3/mmc$ are indirect, direct and indirect, respectively [13].

At room temperature, MgF_2 adopts $P6_3/mmc$. The pressure induced phase of MgF_2 , as shown in Figure 1.5, are in the following order [8]: $P4_2/mmm \rightarrow Pbcn$ (9.4 GPa) $\rightarrow Pa3$ (15.4 GPa) $\rightarrow Pbca$ (39.6 GPa) $\rightarrow Pnma$ (44.1 GPa). Furthermore, it also has high transmittance so it can be used in glass manufacturing [19]. The transmission of MgF_2 is comparable with CaF_2 , see Figure 1.6.

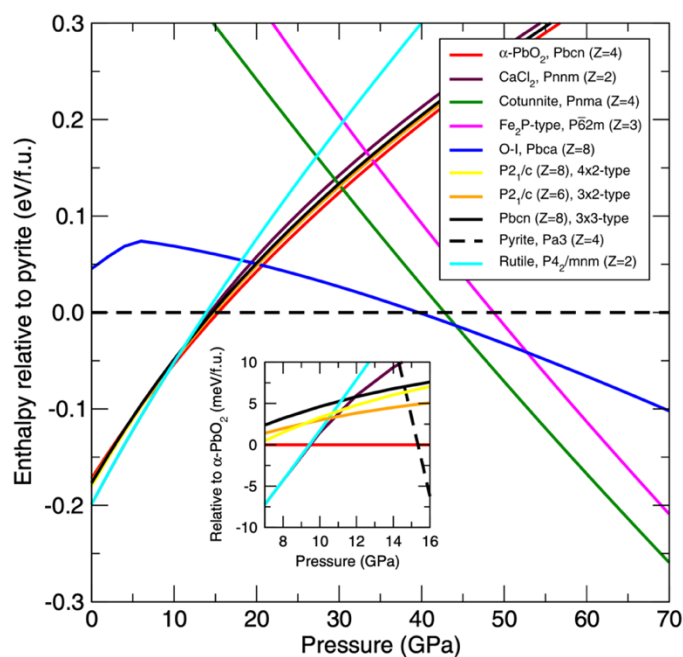


Figure 1.5: Enthalpy of MgF₂ relative to Pyrite against pressure [8]

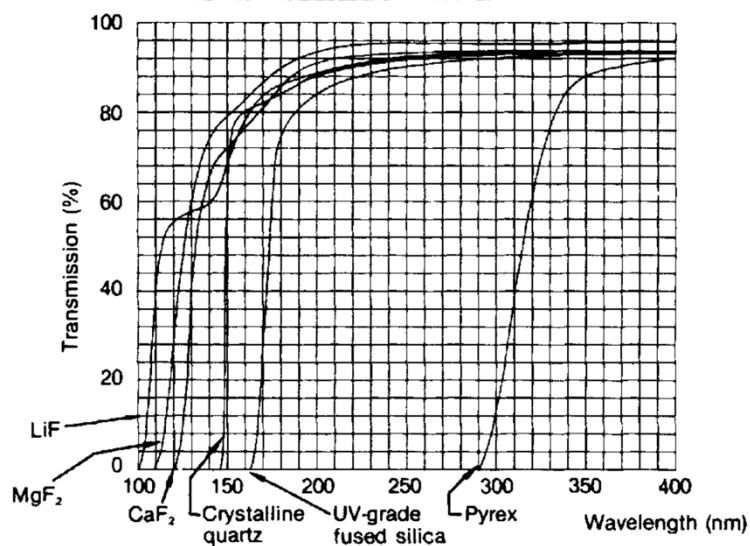


Figure 1.6: The graph of transmission (%) [20]

Since MgF₂ and CaF₂ share the same structure, Pnma, at 70 GPa therefore we chose Mg as a guest for CaF₂ host structure under high pressure. As shown in Figure 1.7, the band gap of MgF₂ is higher the band gap of CaF₂. To prevent collapsing of band gap of CaF₂ at high pressure, we

interested in wide band gap material under high pressure. Sukmas W., *et al.* enhanced superconductivity of metal hydride by doping Mg to the $\text{Mg}_{1-x}\text{Ca}_x\text{H}_6$ system [21].

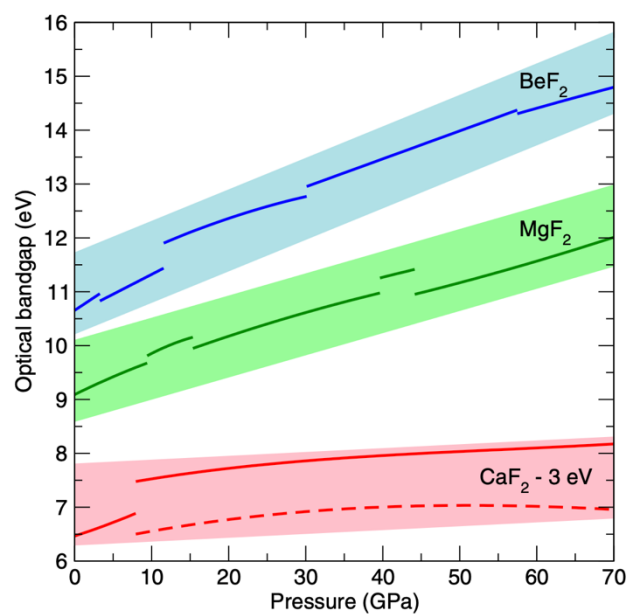
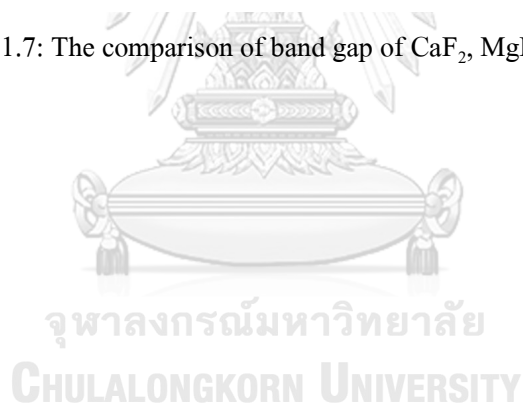


Figure 1.7: The comparison of band gap of CaF_2 , MgF_2 , and BeF_2 [8].



2. THEORETICAL BACKGROUND

By solving a Schrodinger's equation, we can make a good prediction of the behavior of a particle in microscopic world. But the problem arises when we want to solve for the exact solution of a large interacting system containing more than 10^{23} atoms because of the computational costs and errors in predictions. However, the time-independent Schrodinger equation of the interacting system can be written as

$$\hat{H}\Psi(r_1, r_2, \dots, r_n, R_1, R_2, \dots, R_N) = E\Psi(r_1, r_2, \dots, r_n, R_1, R_2, \dots, R_N) \quad (2.1)$$

Where \hat{H} is the Hamiltonian operator of the interacting system

$$\hat{H} = -\frac{1}{2} \sum_{i=1}^n \nabla_i^2 - \frac{1}{2} \sum_{I=1}^N \frac{1}{M_I} \nabla_I^2 - \sum_{i,I} \frac{Z_I}{|\mathbf{r}_i - \mathbf{R}_I|} + \frac{1}{2} \sum_{i \neq j} \frac{1}{|\mathbf{r}_i - \mathbf{r}_j|} + \frac{1}{2} \sum_{I \neq J} \frac{Z_I Z_J}{|\mathbf{R}_I - \mathbf{R}_J|} \quad (2.2)$$

The right hand side of Eq. (2.2) defines, in sequence, the kinetic energy of electrons, the kinetic energy of nuclei, Coulomb interactions between electron and nuclei, Coulomb interactions between electron and electron and, Coulomb interactions between nuclei and nuclei. From the Born-Oppenheimer approximation [22], the contribution of kinetic term of the nuclei in Eq. (2.2) can be neglected because their weight are 10^3 times of electron so they are fixed in the space relative to moving electrons. And the coulomb interaction between nuclei and nuclei term can be taken as a constant. Then the problem is simplified to system of the electron interacting with each other. Now, Eq. (2.1) and (2.2) can be written as

$$\hat{H}\Psi(r_1, r_2, \dots, r_n) = E\Psi(r_1, r_2, \dots, r_n) \quad (2.3)$$

$$\hat{H} = -\frac{1}{2} \sum_{i=1}^n \nabla_i^2 - \sum_{i,I} \frac{Z_I}{|\mathbf{r}_i - \mathbf{R}_I|} + \frac{1}{2} \sum_{i \neq j} \frac{1}{|\mathbf{r}_i - \mathbf{r}_j|} \quad (2.4)$$

The main goal of the density functional theory is to obtain the ground state energy of system because this energy contains all information of the system i.e. position of nuclei which can be used to calculate the next excited state and electronic properties of the system. But still the energy, so-called Hartree energy, calculated from Eq. (2.1) is not giving us true ground state energy so many techniques have been employed to minimize the energy. In 1928, Hartree and Fock [23] proposed that wave function of the electrons must be written as a determinant or antisymmetric wave function to satisfy the Pauli exclusion principle.

$$\Psi_{\text{HF}} = \frac{1}{N!} \det \begin{bmatrix} \psi_1(\mathbf{r}_1) & \psi_2(\mathbf{r}_1) & \dots & \psi_N(\mathbf{r}_1) \\ \psi_1(\mathbf{r}_2) & \psi_2(\mathbf{r}_2) & \dots & \psi_N(\mathbf{r}_2) \\ \vdots & \vdots & \ddots & \vdots \\ \psi_1(\mathbf{r}_N) & \psi_2(\mathbf{r}_N) & \dots & \psi_N(\mathbf{r}_N) \end{bmatrix} \quad (2.5)$$

Now, this determinant named ‘‘Slater determinant’’ includes the permutation effect of the electrons which lower the Hartree energy from Eq. (2.3). The different amount of energy between Hartree method and HF is called ‘‘exchange energy’’. According to Figure 2.1, we still need ‘‘correlation energy’’ introduced in the next section to achieve the true ground state energy of the system.

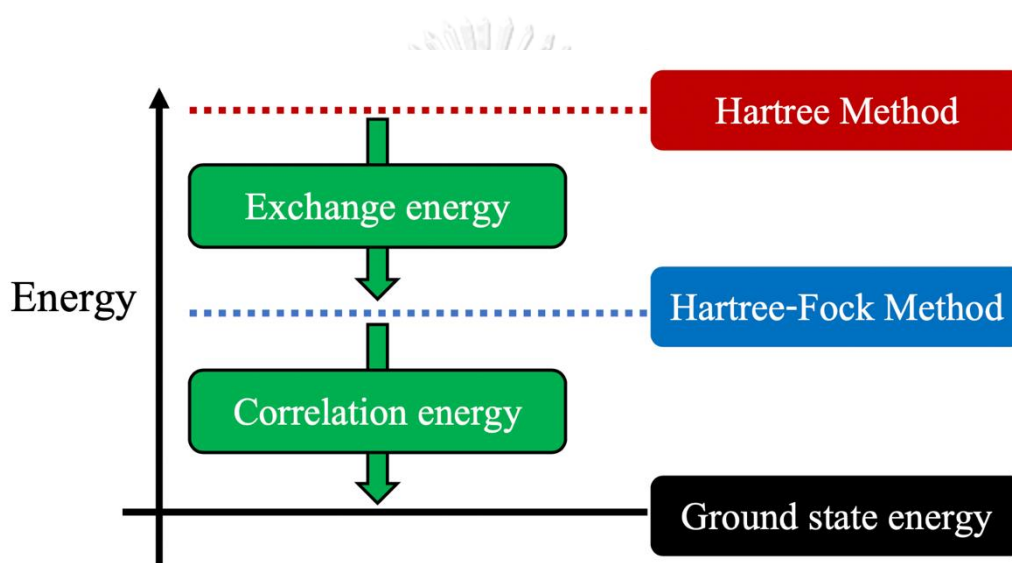


Figure 2.1: shows the energy we need to lower to obtain the true ground state energy

However, both Hartree method and HF method are wave function-based calculation. For large system ($N \gg 6.02 \times 10^{23}$), these methods consume too many computational resources and are impossible to solve because $3N$ -schrodinger equations are needed to be solved and electron-electron interaction terms in Eq. (2.4) are too complicated to solve. To lower the computational cost and to improve the calculations, we need the density functional theory to solve the many electron problems.

2.1 Density functional theory

The density functional theory introduced by Hohenberg and Kohn in 1964 [24] is electron density-based calculation. Therefore, instead of solving 3N-spatial dimension of electronic wave functions, 3-spatial dimension of electron density is used to find the true ground state energy of the system which simplify the problem but yet remain the correction of the calculations. Hohenberg and Kohn have stated two theorems governing DFT calculations.

2.1.1 Hohenberg-Kohn existence theorem

This theorem states that for the ground state density, n_0 , there is one-to-one correspondence between the external potential or potential from nuclei and electron density. Suppose we have two different external potentials, V_a and V_b , which correspond to the same ground state density, n_0 . The difference of external potentials imply that we must have two different Hamiltonian, \hat{H}_a and \hat{H}_b , and also different wave functions, $\Psi_{0,a}$ and $\Psi_{0,b}$. From the variational theorem, we see that the ground state energy of a must be lower than the expectation value of \hat{H}_a over the wave function b.

$$E_{0,a} < \langle \Psi_{0,b} | \hat{H}_a | \Psi_{0,b} \rangle \quad (2.6)$$

$$\text{Where } \hat{H}_a = T + V_{ee} + V_a \text{ and } \hat{H}_b = T + V_{ee} + V_b \quad (2.7)$$

Using the variational theorem and Eq. (2.7), we can write Eq. (2.6) as

$$\begin{aligned} E_{0,a} &< \langle \Psi_{0,b} | \hat{H}_a - \hat{H}_b + \hat{H}_b | \Psi_{0,b} \rangle \\ E_{0,a} &< \langle \Psi_{0,b} | \hat{H}_a - \hat{H}_b | \Psi_{0,b} \rangle + \langle \Psi_{0,b} | \hat{H}_b | \Psi_{0,b} \rangle \\ E_{0,a} &< \langle \Psi_{0,b} | \hat{V}_a - \hat{V}_b | \Psi_{0,b} \rangle + E_{0,b} \\ E_{0,a} &< \int [V_a(\mathbf{r}) - V_b(\mathbf{r})] n_0(\mathbf{r}) d\mathbf{r} + E_{0,b} \end{aligned} \quad (2.8)$$

Then we switch index a in Eq. (2.8) to b and b to a

$$E_{0,b} < \int [V_b(\mathbf{r}) - V_a(\mathbf{r})] n_0(\mathbf{r}) d\mathbf{r} + E_{0,a} \quad (2.9)$$

Adding Eq. (2.8) and (2.9), we obtain

$$E_{0,a} + E_{0,b} < E_{0,a} + E_{0,b} \quad (2.10)$$

Now, we get the contradiction, so called *reductio ad absurdum*, because the left hand side and the right hand side of Eq. (2.10) must be equal. In other words, two different external potentials can't have the same ground state density or the ground state density uniquely determines external potential, Hamiltonian operator and all electronic properties of the system. We can express a ground state energy as a functional of true ground state electron density.

$$\begin{aligned} E_0[n_0] &= T[n_0] + V_{ee}[n_0] + V_{Ne}[n_0] \\ E_0[n_0] &= T[n_0] + V_{ee}[n_0] + \int [V_{Ne}(\mathbf{r})] n_0(\mathbf{r}) d\mathbf{r} \end{aligned} \quad (2.11)$$

The expression in the right hand side of Eq.(2.11) can be divided into two parts that correspond to the Coulomb interaction between electron and nuclei or the system dependent part and the universal part called the Hohenberg-Kohn functional $F_{HK}[n_0]$. Now Eq. (2.11) can be rewritten as

$$E_0[n_0] = F_{HK}[n_0] + \int [V_{Ne}(\mathbf{r})] n_0(\mathbf{r}) d\mathbf{r} \quad (2.12)$$

2.1.2 Hohenberg-Kohn variational theorem

From the Hohenberg-Kohn existence theorem, we are able to construct the ground state electron density. And how can we know that the ground state electron density is the true ground state electron density. To verify that, the variational principle is used. Suppose we use an input in energy functional as a trial electron density n' . Then

$$\langle \Psi' | \hat{H} | \Psi' \rangle = E_0[n'] = T[n'] + V_{Ne}[n'] + V_{ext}[n'] \geq E_0[n_0] = \langle \Psi_0 | \hat{H} | \Psi_0 \rangle \quad (2.13)$$

So this theorem states that for a trial density function n' , the energy functional $E_0[n']$ are always more than the true ground state energy functional $E_0[n_0]$ if the input in energy functional isn't a true ground state electron density.

2.2 The Kohn-Sham Energy

Another brilliant idea of Hohenberg of Kohn is that they turn many electrons problems interacting with each other into many one electron problems. Therefore, the energy of the system is separated into an exact term calculated from noninteracting reference system without using DFT and a

small term approximated by a functional. Now the real kinetic energy of electron consists of a reference term and a term deviated from reference.

$$\langle T[n_0] \rangle_{\text{real}} \equiv \langle T[n_0] \rangle_{\text{ref}} + \Delta \langle T[n_0] \rangle \quad (2.14)$$

With the same idea, we can write the potential energy of electron as

$$\begin{aligned} \langle V_{\text{ee}}[n_0] \rangle_{\text{real}} &\equiv \langle V_{\text{ee}}[n_0] \rangle_{\text{ref}} + \Delta \langle V_{\text{ee}}[n_0] \rangle \\ \langle V_{\text{ee}}[n_0] \rangle_{\text{real}} &\equiv \frac{1}{2} \iint \frac{n_0(\mathbf{r}_1)n_0(\mathbf{r}_2)}{r_{12}} d\mathbf{r}_1 d\mathbf{r}_2 + \Delta \langle V_{\text{ee}}[n_0] \rangle \end{aligned} \quad (2.15)$$

Substituting Eq. (2.14) and Eq. (2.15) into Eq. (2.11)

$$\begin{aligned} E_0[n_0] &= \langle T[n_0] \rangle_{\text{ref}} + \Delta \langle T[n_0] \rangle + \frac{1}{2} \iint \frac{n_0(\mathbf{r}_1)n_0(\mathbf{r}_2)}{r_{12}} d\mathbf{r}_1 d\mathbf{r}_2 + \Delta \langle V_{\text{ee}}[n_0] \rangle + \\ &\quad \int [V_{\text{Ne}}(\mathbf{r})] n_0(\mathbf{r}) d\mathbf{r} \end{aligned} \quad (2.16)$$

Now the exchange correlation energy can be introduced by sum of the kinetic energy deviation and the potential energy deviation.

$$E_{\text{XC}}[n_0] \equiv \Delta \langle T[n_0] \rangle + \Delta \langle V_{\text{ee}}[n_0] \rangle \quad (2.17)$$

Hence Eq. (2.16) can be expressed as

$$E_0[n_0] = \langle T[n_0] \rangle_{\text{ref}} + \frac{1}{2} \iint \frac{n_0(\mathbf{r}_1)n_0(\mathbf{r}_2)}{r_{12}} d\mathbf{r}_1 d\mathbf{r}_2 + \int [V_{\text{Ne}}(\mathbf{r})] n_0(\mathbf{r}) d\mathbf{r} + E_{\text{XC}}[n_0] \quad (2.18)$$

The challenging problem in DFT is to find the good approximation of exchange correlation energy because this energy containing all the unknown quantum mechanical information can't be directly calculated. And two of the most popular approximations are Local density approximation and Generalised gradient approximation which will be introduced in the next section. The next crucial task for searching a true ground state density is to find the Kohn-Sham orbital which is the one-electron noninteracting wave function. For noninteracting reference system in an external potential $V_{\text{Ne}}(\mathbf{r})$, the Hamiltonian operator for N-noninteracting electrons can be written as

$$h_i^{\text{KS}} = -\frac{\hbar^2}{2m_e} \nabla_i^2 + V_{\text{ref}}(\mathbf{r}_i) \quad (2.19)$$

and the eigenfunctions for this operator are one electron Kohn-Sham orbitals $\Psi_m^{\text{KS}}(\mathbf{r}_i)$

$$h_i^{\text{KS}} \Psi_m^{\text{KS}}(\mathbf{r}_i) = \epsilon_m^{\text{KS}} \Psi_m^{\text{KS}}(\mathbf{r}_i) \quad (2.20)$$

2.3 The exchange-correlation functional

2.3.1 Local Density Approximation (LDA)

This approximation is assumed that the charge density varies slowly so each small volume turns to be a uniform electron gas. But, by assuming that the electron density is homogeneous is pretty unreal in the real world calculations because the density of the electron of the real system rapidly changes along the coordinates system. Therefore, this approximation is suitable for simple system such as sodium. Moreover, exchange-correlation functional of uniform gas is the only exact solution that we know in DFT so this is why LDA is very important. The local density approximation can be simply expressed as

$$E_{XC}^{LDA}[n(\mathbf{r})] = \int n(\mathbf{r}) \varepsilon_{XC}^{hom}[n(\mathbf{r})] d\mathbf{r} \quad (2.21)$$

Where, $\varepsilon_{XC}^{hom}[n(\mathbf{r})]$ is the exchange-correlation energy per particle of a homogeneous electron density. This functional term can be separated into exchange and correlation parts

$$\varepsilon_{XC}^{hom}[n(\mathbf{r})] = \varepsilon_X^{hom}[n(\mathbf{r})] + \varepsilon_C^{hom}[n(\mathbf{r})] \quad (2.22)$$

the exchange part derived by Bloch and Dirac was found to be [25]

$$\varepsilon_X^{hom}[n(\mathbf{r})] = -\frac{3}{4} \left[\frac{3n(\mathbf{r})}{\pi} \right]^{1/3} \quad (2.23)$$

But the correlation part, $\varepsilon_C^{hom}[n(\mathbf{r})]$, cannot be explicitly expressed so interpolations was done by many groups of researcher. However, in 1980, Ceperly et al. predicted the highly accurate numerical solution of the correlation part by using Monte Carlo method along with Green's function [26]

2.3.2 Generalised Gradient Approximation (GGA)

To handle the drastic change in realistic electron density, the gradient operator should be applied to the approximation at each point. Therefore, GGA is suitable for a complex system. Now, GGA can be expressed as

$$E_{XC}^{GGA}[n(\mathbf{r})] = \int n(\mathbf{r}) \varepsilon_{XC}^{GGA}[n(\mathbf{r}), \nabla n(\mathbf{r})] d\mathbf{r} \quad (2.24)$$

In this thesis, GGA of Perdew-Burke-Ernzerhof have been employed in CASTEP for an exchange-correlation functional [27].

2.4 The Kohn-Sham Equation

By applying the variational theorem to Eq. (2.16), we start to derive the Kohn-Sham equation.

$$0 = \frac{\delta}{\delta n_0} \left(E_0[n_0] - \lambda \int [V_{Ne}(\mathbf{r})] n_0(\mathbf{r}) d\mathbf{r} \right) \quad (2.25)$$

By taking variational derivative each term in Eq. (2.25), we can have

$$\lambda = V_{eff}(\mathbf{r}) + \frac{\delta \langle T[n_0] \rangle_{ref}}{\delta n_0} \quad (2.26)$$

Where

$$V_{eff}(\mathbf{r}) = V_{Ne}(\mathbf{r}) + \frac{\delta J[n_0]}{\delta n_0} + \frac{\delta E_{XC}[n_0]}{\delta n_0} \quad (2.27)$$

And

$$\frac{\delta J[n_0]}{\delta n_0} = J_0 \iint \frac{n_0(\mathbf{r}')}{|\mathbf{r}-\mathbf{r}'|} d\mathbf{r}' \quad (2.28)$$

And

$$\frac{\delta E_{XC}[n_0]}{\delta n_0} = V_{XC}(\mathbf{r}) \quad (2.29)$$

Substituting Eq. (2.28) and Eq. (2.29) into Eq. (2.27)

$$V_{eff}(\mathbf{r}) = V_{Ne}(\mathbf{r}) + J_0 \iint \frac{n_0(\mathbf{r}')}{|\mathbf{r}-\mathbf{r}'|} d\mathbf{r}' + V_{XC}(\mathbf{r})$$

After $V_{ref}(\mathbf{r}_i)$ in Eq.(2.19) is replace by $V_{eff}(\mathbf{r}_i)$. Eq. (2.20) is now

$$\left[-\frac{\hbar^2}{2m_e} \nabla_i^2 + V_{Ne}(\mathbf{r}) + J_0 \iint \frac{n_0(\mathbf{r}')}{|\mathbf{r}-\mathbf{r}'|} d\mathbf{r}' + V_{XC}(\mathbf{r}) \right] \Psi_m^{KS}(\mathbf{r}_i) = \epsilon_m^{KS} \Psi_m^{KS}(\mathbf{r}_i) \quad (2.30)$$

We arrive at Kohn-Sham equation. So if we want to find the true ground state density, we must solve the Kohn-Sham equation. And the DFT workflow is shown in Figure 2.2.

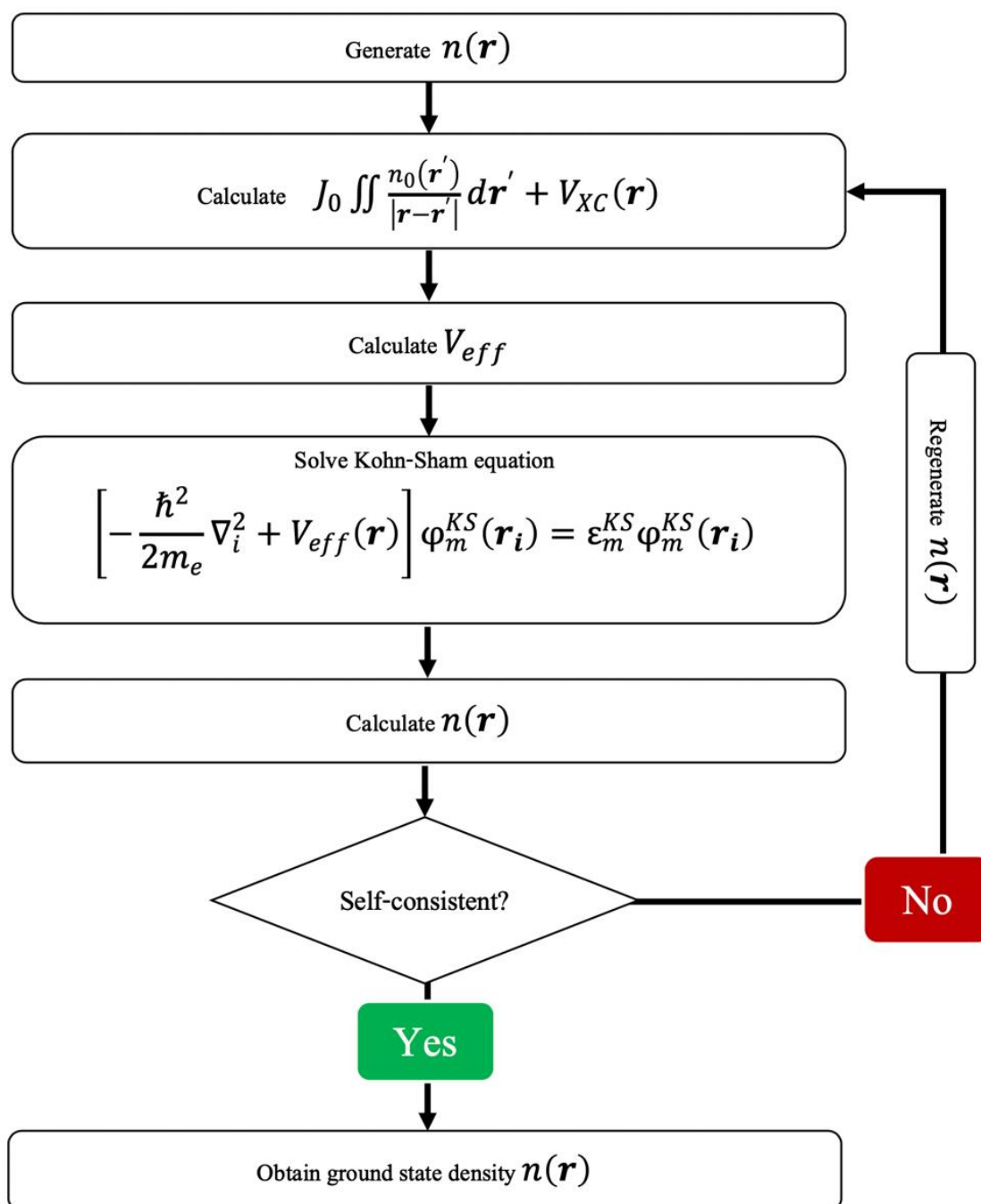


Figure 2.2: Scheme showing the DFT workflow.

2.5 The secular equation

To solve Kohn-Sham equation, Kohn-Sham orbital in Eq.(2.30) must be expanded as a Fourier series where the basis function is arbitrary $\varphi_m^{KS}(\mathbf{r}_i)$.

$$\Psi_m^{KS}(\mathbf{r}_i) = \sum_{i=1}^{\infty} C_i^m \varphi_m^{KS}(\mathbf{r}_i) \quad (2.31)$$

And the coefficients C_i^m are to be determined in secular equations. Moreover, the sum approaching to infinity is needed to improve the accuracy of the approximated Kohn-Sham orbital.

Next, we substitute Eq. (2.31) in Eq. (2.30)

$$\sum_{i=1}^{\infty} C_i^m \left[-\frac{\hbar^2}{2m_e} \nabla_i^2 + V_{\text{eff}}(\mathbf{r}) \right] \varphi_m^{KS}(\mathbf{r}_i) = \sum_{i=1}^{\infty} C_i^m \varepsilon_m^{KS} \varphi_m^{KS}(\mathbf{r}_i) \quad (2.32)$$

Then, we multiply the complex conjugate of $\varphi_m^{KS}(\mathbf{r}_i)$ to the both side of Eq.(2.32) and integrate the entire space. We arrive at

$$\sum_{i=1}^{\infty} C_i^m \int \varphi_m^{*KS}(\mathbf{r}_i) \left[-\frac{\nabla_i^2}{2} + V_{\text{eff}}(\mathbf{r}) \right] \varphi_m^{KS}(\mathbf{r}_i) d\mathbf{r} = \sum_{i=1}^{\infty} C_i^m \varepsilon_m^{KS} \int \varphi_m^{*KS}(\mathbf{r}_i) \varphi_m^{KS}(\mathbf{r}_i) d\mathbf{r} \quad (2.33)$$

Now, Eq. (2.33) turns out to be a matrix. Where the left hand side composes of the Hamiltonian matrix, H, and the coefficients matrix, C. For the right hand side, we have the overlap matrix, S, the coefficients matrix, C, and the diagonal matrix, ε . Therefore, the matrix form, so-called secular determinant, of Eq. (2.33) is

$$HC = SC\varepsilon \quad (2.34)$$

After this matrix is solved, we'll obtain energy roots and coefficients of the basis sets which will be used for further calculations.

2.6 Techniques of DFT calculation

2.6.1 Plane wave basis set

In 1928, Felix Bloch stated that the crystal momentum is conserved if the system is periodic or has translation and rotation invariance. Hence the electron in perfect crystal, or periodic potential, can be expressed as a Bloch's wave [28]

$$\Psi_m^{KS}(\mathbf{r}) = u_m^{KS} e^{i\mathbf{k}\cdot\mathbf{r}} \quad (2.35)$$

Where u_m^{KS} is a periodic function which can be represented as a sum or an integral form of reciprocal lattice vector.

$$\begin{aligned} u(\mathbf{r}) &= \sum_{\mathbf{k}} u_{\mathbf{k}} e^{i\mathbf{k}\cdot\mathbf{r}} \\ u(\mathbf{r}) &= \frac{V}{(2\pi)^3} \int d\mathbf{k} u_{\mathbf{k}} e^{i\mathbf{k}\cdot\mathbf{r}} \end{aligned} \quad (2.36)$$

Then the completed Bloch's wave function can be obtained from Eq. (2.35) and Eq.(2.36)

$$\Psi_m^{KS}(\mathbf{r}) = \sum_{\mathbf{k}} u_{G,\mathbf{k}}(\mathbf{k}) e^{i(\mathbf{k}+\mathbf{G})\cdot\mathbf{r}} \quad (2.37)$$

This function ensures that the electronic wave function and energy are under translational invariance in real space and reciprocal space. So we have

$$\begin{aligned} u(\mathbf{r}) &= u(\mathbf{r}+\mathbf{R}) \\ \Psi(\mathbf{r}) &= \Psi(\mathbf{r}+\mathbf{R}) \\ u(\mathbf{k}) &= u(\mathbf{k}+\mathbf{G}) \end{aligned} \quad (2.38)$$

Where \mathbf{r} and \mathbf{k} represent the lattice vectors and reciprocal lattice vector. Index n represents band index. In other words, if an electron is surrounded by the periodic potential coming from nuclei we can use Bloch's theorem can be used to describe such a system. But this theorem may fail to describe the real solid because real solid has many defects causing no translational and rotational invariance and a problem in solving Kohn-Sham equation. The schrodinger equation governing such a system can be written as

$$\left[\frac{p_i^2}{2m} + V(\mathbf{r}) \right] \Psi_m^{KS}(\mathbf{r}) = E \Psi_m^{KS}(\mathbf{r}) \quad (2.39)$$

After applying momentum operator and Fourier transform to Eq. (2.39). We arrive at

$$\sum_{\mathbf{G}} V_{\mathbf{G}} \Psi_{\mathbf{k}-\mathbf{G}} = \left[E - \frac{\hbar^2 |\mathbf{k}|^2}{2m} \right] \Psi_{\mathbf{k}} \quad (2.40)$$

Now let us consider only kinetic energy term of Eq.(2.40), this term directly corresponds to kinetic cutoff energy if $\mathbf{k} = \mathbf{G}_{max}$. So the kinetic cutoff energy is

$$\varepsilon_{max} = \frac{\hbar^2 |\mathbf{G}_{max}|^2}{2m} \quad (2.41)$$

2.6.2 Pseudopotentials and Projection augmented Wave

Consider a wave function of an electron moving past an ion core, it is accelerated towards the positive ion core due to the real attractive potential energy. The electron gains kinetic energy, which represented as effective repulsive potential energy, so it rapidly oscillates near ion core this fast oscillation lead to abruptly decreasing of electron density, called orthogonality hole. This is the well-known Pauli-exclusion principle since the electron state must be excluded from the core state. Within the core radius, the electron would feel a small amount of potential energy which is called pseudopotential, the combination of the effective repulsive potential and the real attractive potential. Furthermore, the degrees of freedom in Hamiltonian are reduced by the effective potential so the number of electrons in the system is also reduced. Thus, pseudopotential provides us faster calculation.

In real solid, the wave functions of the electrons oscillate with different frequency depending on regions. Near nuclei, it oscillates with very high frequency because of the strong attractive of the nuclei. Conversely, it oscillates with low frequency in the bonding region. This causes a problem in determining Fourier coefficients of the wave function. Now, the pseudopotential is introduced to capture both slow and fast variation of the wave function for all region. This method split the single valence state into smooth wave function, $|\Phi\rangle$, and the summation of core states [29, 30]. Now, we have

$$|\Psi\rangle = |\Phi\rangle + \sum_n \langle x_n | \Psi \rangle |x_n\rangle \quad (2.42)$$

$|\Phi\rangle$ can be represented as plane wave. Then we apply bra of core state and realize that the core state is orthogonal to the smooth wave function, we arrive at

$$\langle x_n | \Psi \rangle = a_n \quad (2.43)$$

The reason why sphere is constructed around the core is that the coulomb potential has spherical symmetry. So we assume that the atom is isolated and has spherical symmetric potential. And each sphere containing nuclei cannot touch the other spheres. So there are two regions: the region inside each sphere and the region in between spheres.

$$\langle r | \hat{t} | r' \rangle = \delta(r-r') \quad (2.44)$$

To fulfill the Eq. (2.44), we must use two different basis. After the two basis are found, we can define the smooth wave function, $|\tilde{\Psi}\rangle$, and true wave function, $|\Psi\rangle$, as the following expressions

$$|\tilde{\Psi}\rangle = \sum_j c_j^a |\tilde{\Phi}_j^a\rangle \quad (2.45)$$

$$|\Psi\rangle = \sum_j c_j^a |\Phi_j^a\rangle \quad (2.46)$$

The coefficients, c_j^a , of Eq.(2.45) and Eq.(2.46) are the same to ensure that two wave functions are equivalent in the outside. Let us consider the radius $r = r_c$, core radius, of each sphere, there are two boundary conditions needed to be fulfilled. First, the smooth wave function must be differentiable. Second, it must be matched with the true wave function. In other words, we want to transform true wave functions living inside the sphere into the smooth wave functions. This transformation is depicted in Figure 2.3.

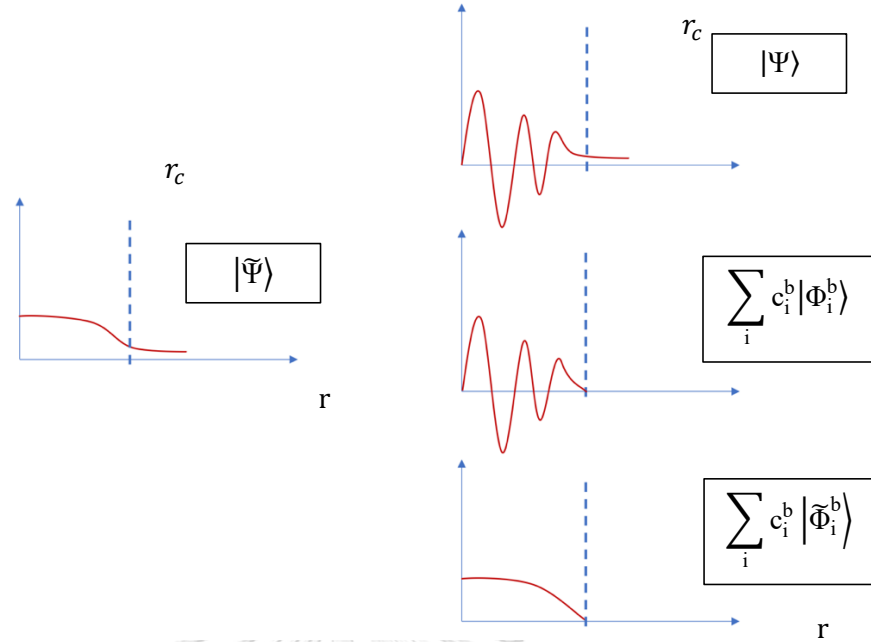


Figure 2.3: shows how to transform the true wave function into the smooth wave function by subtracting non smooth part and adding smooth part to the true wave function.

So we employ linear transformation, \hat{T} .

$$\hat{T} = 1 + \sum_{bi} (|\tilde{\Phi}_i^b\rangle - |\Phi_i^b\rangle) \langle p_i^b| \quad (2.47)$$

The last term of Eq. (2.47) must have the completeness relation

$$\sum_{bi} |\Phi_i^b\rangle \langle p_i^b| = 1 \quad (2.48)$$

And

$$\langle p_i^b | \Phi_j^a \rangle = \delta_{ij} \delta_{ab} \quad (2.49)$$

Operating \hat{T} to true wave function, Eq.(2.46).

$$\begin{aligned} \hat{T}|\Psi\rangle &= |\Psi\rangle + \sum_{bi} (|\tilde{\Phi}_i^b\rangle - |\Phi_i^b\rangle) \langle p_i^b| \sum_{ja} c_j^a |\Phi_j^a\rangle \\ \hat{T}|\Psi\rangle &= |\Psi\rangle + \sum_{bi} (|\tilde{\Phi}_i^b\rangle - |\Phi_i^b\rangle) \sum_{ja} c_j^a \delta_{ij} \delta_{ab} \\ \hat{T}|\tilde{\Psi}\rangle &= |\Psi\rangle - \sum_i c_i^b |\Phi_i^b\rangle + \sum_i c_i^b |\tilde{\Phi}_i^b\rangle \\ \hat{T}|\Psi\rangle &= |\tilde{\Psi}\rangle \end{aligned} \quad (2.50)$$

From the above derivation, we can now derive the all operators, i.e. kinetic energy operator, potential energy operator, and, density operator, which will be used for the Kohn-Sham equation. We start by writing the expectation value of the true wave function in term of smooth wave function.

$$\langle \Psi_m | \hat{O} | \Psi_n \rangle = \langle \tilde{\Psi}_m | \hat{T}^\dagger \hat{O} \hat{T} | \tilde{\Psi}_n \rangle \quad (2.51)$$

We operate \hat{T} on $|\tilde{\Psi}_n\rangle$ and \hat{T}^\dagger on $\langle \tilde{\Psi}_m|$, then we obtain

$$\begin{aligned} \langle \Psi_m | \hat{O} | \Psi_n \rangle = & \langle \tilde{\Psi}_m | \hat{O} | \tilde{\Psi}_n \rangle + \sum_{aibj} c_{ni}^a c_{mj}^{b*} \langle \Phi_j^b - \tilde{\Phi}_j^b | \hat{O} | \Phi_i^a - \tilde{\Phi}_i^a \rangle + \sum_{aibj} c_{mj}^{b*} \langle \Phi_j^b - \tilde{\Phi}_j^b | \hat{O} | \tilde{\Psi}_n \rangle \\ & + \sum_{aibj} c_{ni}^a \langle \tilde{\Psi}_m | \hat{O} | \Phi_i^a - \tilde{\Phi}_i^a \rangle \end{aligned} \quad (2.52)$$

Now, we obtain the general operator for any expectation value. $\langle \Phi_j^b - \tilde{\Phi}_j^b | \hat{O} | \Phi_i^a - \tilde{\Phi}_i^a \rangle$ from above equation will be vanished if they're in different sphere. So

$$\langle \Phi_j^b - \tilde{\Phi}_j^b | \hat{O} | \Phi_i^a - \tilde{\Phi}_i^a \rangle = \delta_{ab} \quad (2.53)$$

Applying Eq. (2.53) to Eq. (2.52)

$$\begin{aligned} \langle \Psi_m | \hat{O} | \Psi_n \rangle = & \langle \tilde{\Psi}_m | \hat{O} | \tilde{\Psi}_n \rangle + \sum_{aibj} c_{ni}^a c_{mj}^{a*} (\langle \Phi_j^a | \hat{O} | \Phi_i^a \rangle - \langle \tilde{\Phi}_j^a | \hat{O} | \tilde{\Phi}_i^a \rangle) \\ \langle \tilde{\Psi}_m | \hat{T}^\dagger \hat{O} \hat{T} | \tilde{\Psi}_n \rangle = & \langle \tilde{\Psi}_m | \hat{O} | \tilde{\Psi}_n \rangle + \sum_{aibj} c_{ni}^a c_{mj}^{a*} (\langle \Phi_j^a | \hat{O} | \Phi_i^a \rangle - \langle \tilde{\Phi}_j^a | \hat{O} | \tilde{\Phi}_i^a \rangle) \end{aligned} \quad (2.54)$$

We can pull the operator out of Eq. (2.54),

$$\hat{T}^\dagger \hat{O} \hat{T} = \hat{O} + \sum_{aibj} |\tilde{p}_j^b\rangle (\langle \Phi_j^a | \hat{O} | \Phi_i^a \rangle - \langle \tilde{\Phi}_j^a | \hat{O} | \tilde{\Phi}_i^a \rangle) \langle \tilde{p}_i^a| \quad (2.55)$$

From Eq. (2.55), we then can represent the kinetic energy operator

$$\hat{T}^\dagger \hat{T} = -\frac{\nabla^2}{2} + \sum_{aibj} |\tilde{p}_j^b\rangle (E_{ij}^{a,kin} - \tilde{E}_{ij}^{a,kin}) \langle \tilde{p}_i^a| = \tilde{t} \quad (2.56)$$

and potential operator can be written as

$$\hat{T}^\dagger \hat{V} \hat{T} = \hat{V} + \sum_{aibj} |\tilde{p}_j^b\rangle (\langle \Phi_j^a | \hat{V} | \Phi_i^a \rangle - \langle \tilde{\Phi}_j^a | \hat{V} | \tilde{\Phi}_i^a \rangle) \langle \tilde{p}_i^a| = \tilde{V} \quad (2.57)$$

Furthermore, the overlapping matrix, \tilde{S} , can also be introduced from Eq.(2.55)

$$\hat{T}^\dagger \hat{T} = \hat{1} + \sum_{aibj} |\tilde{p}_j^b\rangle \langle \Phi_j^a | \hat{1} | \Phi_i^a \rangle - \langle \tilde{\Phi}_j^a | \hat{1} | \tilde{\Phi}_i^a \rangle \langle \tilde{p}_i^a| = \tilde{S} \quad (2.58)$$

The most important term is the density operator which will be used for electron density in Kohn-Sham equation.

$$\begin{aligned} \langle \Psi_m | r \rangle \langle r | \Psi_n \rangle &= \langle \tilde{\Psi}_m | r \rangle \langle r | \tilde{\Psi}_m \rangle + \sum_{aibj} c_{ni}^a c_{mj}^{a*} (\langle \Phi_j^a | r \rangle \langle r | \Phi_i^a \rangle - \langle \tilde{\Phi}_j^a | r \rangle \langle r | \tilde{\Phi}_i^a \rangle) \\ \hat{n} &= \hat{n} + \sum_{aibj} |\tilde{p}_j^b\rangle (\langle \Phi_j^a | r \rangle \langle r | \Phi_i^a \rangle - \langle \tilde{\Phi}_j^a | r \rangle \langle r | \tilde{\Phi}_i^a \rangle) \langle \tilde{p}_i^b | \end{aligned} \quad (2.59)$$

With kinetic energy operator, potential energy operator, overlapping operator, and, density operator, we can construct secular determinant mentioned in Eq. (2.33) to solve the Kohn-Sham equation.

$$(\tilde{H} - \epsilon \tilde{S}) |\tilde{\Psi}\rangle = 0 \quad (2.60)$$

Where \tilde{H} is Hamiltonian matrix, $\tilde{H} = \tilde{t} + \tilde{V}$.

2.6.3 The Ultrasoft pseudopotential

The formalism of projection augmented wave can be used as an input to construct the formalism of ultrasoft pseudopotentials. We operate H on pseudostates, $|\varphi_v^{PS}\rangle$.

$$\left[H + \sum_{\alpha,c} (\epsilon_v - \epsilon_{\alpha,c}) |\varphi_{\alpha,c}\rangle \langle \varphi_{\alpha,c}| \right] |\varphi_v^{PS}\rangle = \epsilon_v^{PS} |\varphi_v^{PS}\rangle \quad (2.61)$$

Where $|\varphi_{\alpha,c}\rangle$ is core state. We then obtain Schrodinger-like equation with pseudostates and the additional potential, V_R .

$$V_R = \sum_{\alpha,c} (\epsilon_v - \epsilon_{\alpha,c}) |\varphi_{\alpha,c}\rangle \langle \varphi_{\alpha,c}| \quad (2.62)$$

Now, the Phillips-Kleinman pseudopotential [31] can be introduced by adding V_R to the original coulomb potential V

$$V_{PK} = V + V_R \quad (2.63)$$

V_R vanishes outside the core region so V_{PK} equals to V. In 1990, Vanderbilt et. al. proposed ultrasoft pseudopotential which is not norm conserving pseudopotential [32]. They proposed that outside the core the pseudo wave functions are set to be all electron wave functions and inside the core the pseudo wave functions are treated as soft as possible. So this method can be done by removing the norm conservation constraint. The upside of this method is that the radius of core is

large so plane wave cutoff is tremendously reduced. Now, the total energy of this approach can be written as

$$E_0 = \sum_j \langle \varphi_j | T + V^{NL} | \varphi_j \rangle + \int V^L n_0(\mathbf{r}) d\mathbf{r} + \frac{1}{2} \iint \frac{n_0(\mathbf{r}_1) n_0(\mathbf{r}_2)}{r_{12}} d\mathbf{r}_1 d\mathbf{r}_2 + E_{xc} + E_{ii} \quad (2.64)$$

Where V^{NL} is nonlocal Vanderbilt pseudopotential, V^L is local pseudopotential, φ_j are pseudo wave functions. V^{NL} for one atom can be expressed as

$$V^{NL} = \sum_{nm} D_{nm}^{(0)} |\beta_n\rangle \langle \beta_m| \quad (2.65)$$

Where β_n can be written on term radial wave functions and spherical harmonics. The charge density in ultrasoft pseudopotential formalism is represented by adding an augmentation term inside the sphere to the density of the pseudo wave functions.

$$n(\mathbf{r}) = \sum_{occ} \left[\varphi_j^*(\mathbf{r}) \varphi_j(\mathbf{r}) + \sum_{nm} Q_{nm}(\mathbf{r}) \langle \varphi_j | \beta_n \rangle \langle \beta_m | \varphi_j \rangle \right] \quad (2.66)$$

Where $Q_{nm}(\mathbf{r})$ are the augmentation functions which is the difference between the density of all electron and pseudo wave functions.

$$Q_{nm}(\mathbf{r}) = \langle \varphi_j^{AE} | \varphi_k^{PS} \rangle - \langle \varphi_j^{PS} | \varphi_k^{PS} \rangle \quad (2.67)$$

we can write the secular equation using the variational principle.

$$(\tilde{H} - \varepsilon_j \tilde{S}) |\tilde{\Psi}\rangle = 0 \quad (2.68)$$

Where

$$\tilde{H} = T + V_{xc}(\mathbf{r}) + V_H(\mathbf{r}) + V^L(\mathbf{r}) + \sum_{nm} D_{nm} |\beta_n\rangle \langle \beta_m| \quad (2.69)$$

And overlapping matrix, S, is

$$\tilde{S} = 1 + \sum_{nm} q_{nm} |\beta_n\rangle \langle \beta_m| \quad (2.70)$$

And

$$q_{nm} = \int_0^{r_c} d\mathbf{r} Q_{nm}(\mathbf{r}) \quad (2.71)$$

We then add screening term to $D_{nm}^{(0)}$ in Eq.(2.69).

$$D_{nm} = D_{nm}^{(0)} + \int_0^{r_c} dr V^L(\mathbf{r}) Q_{nm}(\mathbf{r}) \quad (2.72)$$

2.6.4 Cutoff energy and k-point mesh

In theory, we can have the infinite terms of basis function but it's not feasible for the computational sense. DFT is calculated on reciprocal space. The maximum grid needed for DFT is determined by Cutoff energy. To save the computational cost, we can't compute whole reciprocal space so the kinetic cutoff energy must be determined before performing any DFT calculations.

$$\epsilon_{max} = \frac{\hbar^2 |G_{max}|^2}{2m} \quad (2.77)$$

2.6.5 Geometry optimization

The purpose of geometry optimization is to find particular atomic arrangements that minimize enthalpy of the unit cell [33]. Let us now consider a diatomic, say, its enthalpy depends on the bond length, one dimensional coordinates. We then compress the unit cell and calculate the enthalpy. If the enthalpy keeps decreasing with increasing pressure, we want to keep doing that until it reaches turning point. Then we keep increasing pressure and now the enthalpy should be increased. So what we obtained is a parabolic curve of the enthalpy. In other words, we obtained three adjacent points where the middle point is the lowest enthalpy among the two points. Instead of parabolic curve, we now determine the energy surface of unit cell of crystalline containing 3N-spatial coordinates.

$$\mathcal{H} = \mathcal{H}(\boldsymbol{\epsilon}, \mathbf{s}_1, \dots, \mathbf{s}_n) \quad (2.79)$$

Where $\boldsymbol{\epsilon}_{ij}$ is the nine components of the a point in configuration space represented by column matrix, \mathbf{X} , used to avoid rotation of unit cell and \mathbf{s}_i is spatial coordinates of the atom in the unit cell. Each component of \mathbf{X} can be expressed as

$$X_{3(i-1)+j} = \epsilon_{ij} \quad (2.80)$$

Where $i, j = 1, 2, 3$

The traditional enthalpy can be expressed as $\mathcal{H} = E + pV + TS$. But, Temperature of DFT calculations is based on 0 K so the enthalpy per unit cell is now

$$\mathcal{H} = E + p\Omega \quad (2.81)$$

Where p is pressure and Ω is volume per unit cell. Now The variation of enthalpy around a minima, X_{min} , can be approximated by

$$\delta\mathcal{H} = \frac{1}{2}(X - X_{min})^T \cdot A \cdot (X - X_{min}) \quad (2.82)$$

Where A is Hessian matrix, the matrix of second derivative of the enthalpy.

$$A = \begin{bmatrix} \frac{\partial^2 \mathcal{H}}{\partial x_1 \partial x_1} & \cdots & \frac{\partial^2 \mathcal{H}}{\partial x_1 \partial x_N} \\ \vdots & \ddots & \vdots \\ \frac{\partial^2 \mathcal{H}}{\partial x_N \partial x_1} & \cdots & \frac{\partial^2 \mathcal{H}}{\partial x_N \partial x_N} \end{bmatrix} \quad (2.83)$$

Since, hessian matrix cannot be directly solved so BFGS quasi-Newton schemes [34] is employed to guess for A. The preceding hessian matrix will be used to calculate successively improved one. Then, we move closer to the minimum by each step which can be expressed as

$$X_{i+1} = X_i + \lambda \Delta X_i \quad (2.84)$$

Where λ is a step occasionally taken as 1 and ΔX_i is

$$\Delta X_i = B_i F_i \quad (2.85)$$

The force vector, F_i , can be calculated by taking derivative of Eq.(2.81) with respect to X

$$F = - \left. \frac{\partial \mathcal{H}}{\partial x} \right|_p \quad (2.86)$$

And B is the inverse of A

$$B = A^{-1} \quad (2.87)$$

After this whole calculation is done, all atoms in unit cell are in relaxed position, X_{min} . Therefore, each unit cell also has the lowest enthalpy. In other words, the crystal structure has net interatomic energy close to zero and each atom close to its stationary position.

2.6.6 Cluster expansion

Cluster expansion adopts the idea from Ising model so atom occupied in each site is labeled by spin-like integers, -1 and +1. Let us now consider the magnetic phase transition. Under high temperature, all spins would randomly align so there's no net magnetization. But if the system is cooled down, we would find some region with a group of spins up and spins down because if there's a spin up, the near neighbor should also exhibit spin up and Vice-Versa. Then the same thing happens with binary alloy system. For Mg-Li alloy under high temperature, the Mg and Li atoms would sit in disordered positions. But if we now decrease the temperature, some of Mg and Li atoms would sit in ordered positions. We can say that if we found Mg, there's a high chance that we would find Li and Vice-Versa. Instead of magnetic transition, we consider the order-disorder transition. Therefore, we can find the energy of the binary alloy system, $E^{CE}(\sigma)$, with various atomic arrangements via cluster expansion.

$$E^{CE}(\sigma) = \sum_{\alpha} m_{\alpha} J_{\alpha} \bar{\Pi}_{\alpha}(\sigma) \quad (2.88)$$

Where J_{α} is effective cluster interaction (ECI) and $\bar{\Pi}_{\alpha}(\sigma)$ is correlation matrix accounting for probability of finding cluster α . It can be written as

$$\bar{\Pi}_{\alpha}(\sigma) = \frac{1}{N_{\alpha} m_{\alpha}} \sum_{\beta \equiv \alpha} \prod_{i \in \beta} \sigma_i \quad (2.89)$$

Where σ_i is occupational number taken to be +1 and -1. The value of occupational number depends on the type of atom. N_{α} is number of atoms in the unit cell and m_{α} is number of atomic site of cluster α . Now, we illustrate the two-dimensional binary alloy system for a clear explanation in Figure 2.4.

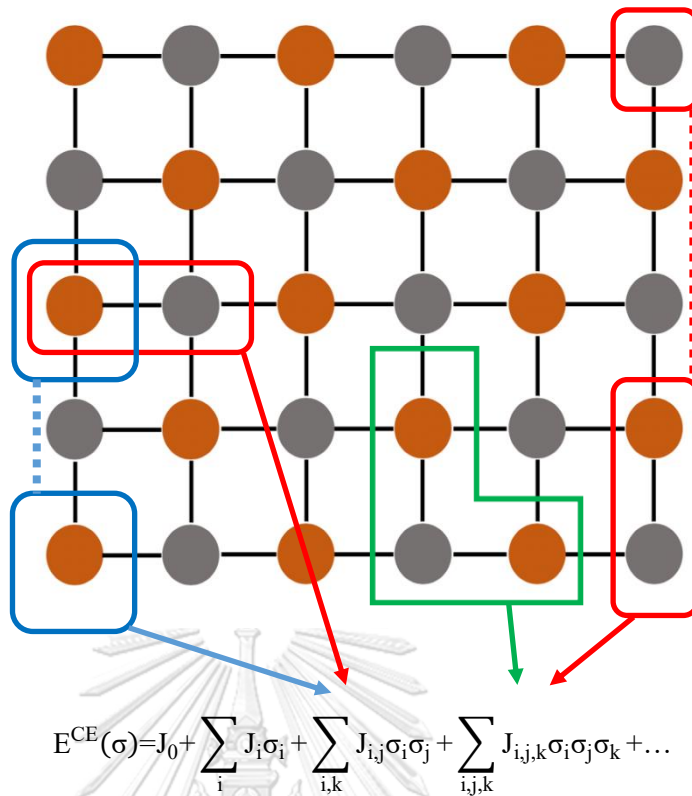


Figure 2.4: Picture of the two sites interactions and the three sites interactions.

The first term, J_0 , is taken to be a constant. The second term is the sum of an atom sitting in each lattice site. The third term represents the sum of a pair of atoms sitting between different two lattice site. This term can be considered between an atom of interest and its nearest neighbor or its next nearest neighbor and so on. But these expansions are never expanded to infinity terms because effective cluster interactions are rapidly decayed if it is too far away from the atom of interest. Then the fourth term is the sum of three sites. So far, the real challenging problem is to determine effective cluster interactions.

2.6.7 Phase transitions

There are many kind of phase transitions such as liquid changing to solid, but in this thesis, we consider the phase transitions induced by pressure. To predict the phase transitions of the solid, we use Birch-Murnaghan equation of states [35, 36]. Now if we plot the graph between Enthalpy and pressure, the phase transition can be determined by the intersection of the enthalpy of two

different phases. The new pressure induced phase will be in new group of symmetry. The enthalpy and pressure can be expressed as

$$E(V) = E_0 + \frac{9V_0B_0}{16} \left\{ B'_0 \left[\left(\frac{V_0}{V} \right)^{2/3} - 1 \right]^3 + \left[\left(\frac{V_0}{V} \right)^{2/3} - 1 \right]^2 \left[6 - 4 \left(\frac{V_0}{V} \right)^{2/3} \right]^3 \right\} \quad (2.90)$$

$$P(V) = \frac{3B_0}{2} \left[\left(\frac{V_0}{V} \right)^{7/3} - \left(\frac{V_0}{V} \right)^{5/3} \right] \left\{ 1 + \frac{3}{4} (B'_0 - 4) \left[\left(\frac{V_0}{V} \right)^{2/3} - 1 \right] \right\} \quad (2.91)$$

Where B_0 is bulk modulus at 0 GPa and B'_0 is first derivative of bulk modulus with respect to pressure at 0 GPa and V_0 is volume at 0 GPa.

2.6.8 Gibbs free energy

The phase transitions of the material under high pressure can be thermodynamically determined from Gibbs free energy.

$$G = E + PV - TS \quad (2.92)$$

Where $H = E + PV$ is enthalpy and S is entropy. In first principle calculation, entropy is set to be zero for convenience purpose so Gibbs free energy is reduced to enthalpy

$$G = E + PV = H \quad (2.93)$$

The first order phase transition of isothermal process is controlled by 2 conditions, $\Delta G = 0$ and $\left(\frac{\partial G}{\partial P} \right)_T = V$. The common tangent line of phase-A and phase-B, as depicted in Figure 2.5, can be interpreted as the pressure at which the phase-A transforms to phase-B. Moreover, the volume between two phase transitions should not be continuous but this volume might be continuous for second order phase transition.

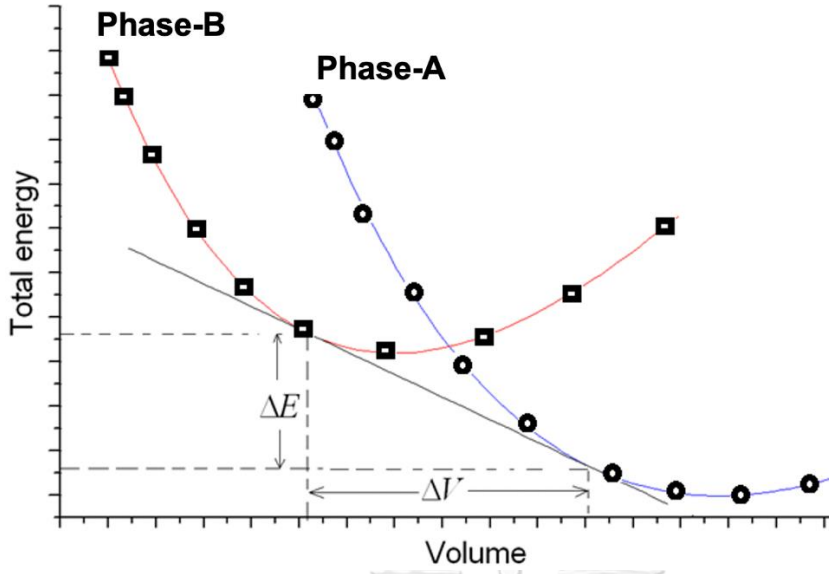


Figure 2.5: Graph of E-V curve in which the common tangential line represents transition pressure.

2.6.9 Phonon dispersion relation

The vibrational energy of all atoms can be written as

$$E = \frac{1}{4} \sum_{n,n'} \sum_{j,j'} (u_{j,n} - u_{j',n'})^2 \phi_{n,n}^{jj'} \quad (2.94)$$

Where $u_{j,n}$ is displacement of j th atom in the n th unit cell and $\phi_{n,n}^{jj'}$ is the second derivative of each bond energy with respect to the displacements of two atoms, which is living in the bond. We can represent the displacement $u_{j,n}$ as traveling wave.

$$u_{j,n} = \tilde{u}_j \exp(i(kna - \omega t)) \quad (2.95)$$

Where \tilde{u}_j is the amplitude of the wave. Next, we take the derivative of Eq. (2.94) with respect to displacement to find the force acting on each atom and take the second derivative of Eq. (2.95) to find acceleration. Then we apply Newton 2nd law to the result. We now obtain the Newton 2nd law of motion for all atoms living in n th unit cell.

$$\omega^2 e_j = \sum_{j',n'} \frac{1}{\sqrt{m_j m_{j'}}} \phi_{n,n}^{jj'} \exp(ik(n'-n)a) e_{j'} \quad (2.96)$$

For simplicity, we can define $e_j = \sqrt{m_j} \tilde{u}_j$. Therefore, Eq. (2.96) can be written in matrix representation

$$\omega^2 \mathbf{e} = \mathbf{D}(\mathbf{k}) \cdot \mathbf{e} \quad (2.97)$$

Where $\mathbf{D}(\mathbf{k})$ is dynamical matrix and \mathbf{e} is column vector of e_j

$$\mathbf{e} = \begin{pmatrix} \vdots \\ e_j \\ \vdots \end{pmatrix} \quad (2.98)$$

After we diagonalize the matrix, we'll obtain the roots (frequencies) of Eq. (2.97). The mechanical stability of a solid structure is governed by these frequencies. If the frequencies are real number, the solid structure is stable but if the frequencies are imaginary number the solid structure is unstable because the atomic displacement contains exponential decay term and the atoms will not oscillate around equilibrium point. All of atoms in unit cell will oscillate in new equilibrium positions when the phase transition is changed to new phase transition.

2.6.10 Band structure

The simulated solid structures in CASTEP have symmetry, depending on the space group, hence we can apply the Bloch theorem to the density functional theory and calculate the electronic structure. The Kohn-Sham equation for the crystal can be written as [37]

$$\left[-\frac{1}{2} (\nabla + i\mathbf{k})^2 + V_{\text{tot}}(\mathbf{r}) \right] u_{i\mathbf{k}}(\mathbf{r}) = \varepsilon_{i\mathbf{k}} u_{i\mathbf{k}}(\mathbf{r}) \quad (2.99)$$

Where i in the subscript of $u_{i\mathbf{k}}$ is the index of eigenstate and i in the Eq.(2.99) is the imaginary unit.

$$\hat{H}_{\mathbf{k}} = -\frac{1}{2} (\nabla + i\mathbf{k})^2 + V_{\text{tot}} \quad (2.100)$$

$$\hat{H}_{\mathbf{k}} u_{i\mathbf{k}} = \varepsilon_{i\mathbf{k}} u_{i\mathbf{k}} \quad (2.101)$$

We then impose the periodic condition, Eq. (2.38), and solve Eq. (2.39). For the convenience purposes, this function is normalized within the volume of one unit cell of the whole unit cells.

$$\int_{\text{UC}} |u_{i\mathbf{k}}(\mathbf{r})|^2 d\mathbf{r} = 1 \quad (2.102)$$

The normalized periodic function guarantee that we can find only one electron in one unit cell. Due to the periodic conditions, we can apply the periodic function to any unit cell in the solid. This saves a large amount of computational cost. After we solve the Kohn-Sham equation of the crystal, we can construct the electron density.

$$n(\mathbf{r}) = \sum_i \int_{\text{BZ}} \frac{d\mathbf{k}}{\Omega_{\text{BZ}}} f_{i\mathbf{k}} |u_{i\mathbf{k}}(\mathbf{r})|^2 \quad (2.103)$$

The integral in Eq. (2.103) is restricted only in the first Brillouin zone (BZ). Ω_{BZ} is the volume of the unit cell in the first Brillouin zone. The occupation number, $f_{i\mathbf{k}}$, can be either one for occupied states or zero for unoccupied states. We then use this electron density to rewrite the total energy of Kohn-Sham equation as the following expression.

$$E = \sum_i \int_{\text{BZ}} \frac{d\mathbf{k}}{\Omega_{\text{BZ}}} f_{i\mathbf{k}} \varepsilon_{i\mathbf{k}} - \left[E_{\text{H}} + \int d\mathbf{r} V_{\text{xc}}(\mathbf{r}) n(\mathbf{r}) - E_{\text{XC}} \right] \quad (2.104)$$

To plot the band structure of the crystal, each discrete i branch of $\varepsilon_{i\mathbf{k}}$ is plotted along continuous wave vector, \mathbf{k} . We can use the band structure to classify the crystal whether it is an insulator, a conductor, or a semiconductor. The band gap is the gap between conduction band and valence band, see Figure 2.6. If the conduction band and valence band are intersected, the crystal is a conductor. If the energy gap between conduction band and valence band is approximately 1 eV, the crystal is a semiconductor. If the energy gap between conduction band and valence band is more than 6 eV, the crystal is an insulator.

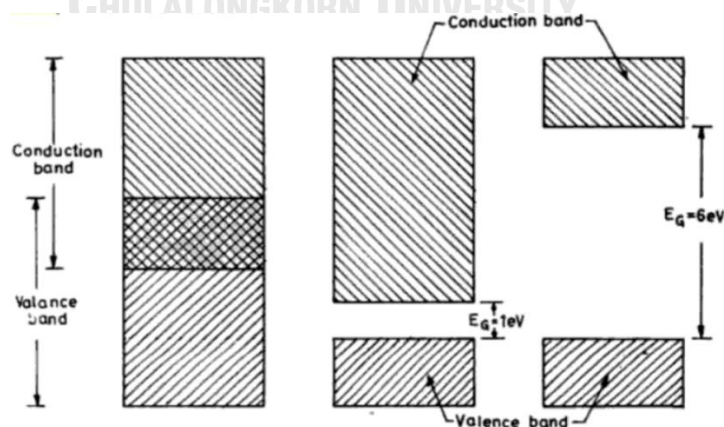


Figure 2.6: Graph of energy gap where (a) is conductor, (b) is a semiconductor, and (c) is an insulator [38]

The gap between conduction band and valence band can be adjusted by applying pressure to the crystal. For instance, the crystal can interchange between an insulator and a metal, see Figure 2.7. The valence band of an insulator is fully occupied by electrons. After applying pressure to the crystal, the gap is narrowed and some electrons move to conduction band so the crystal is metal.

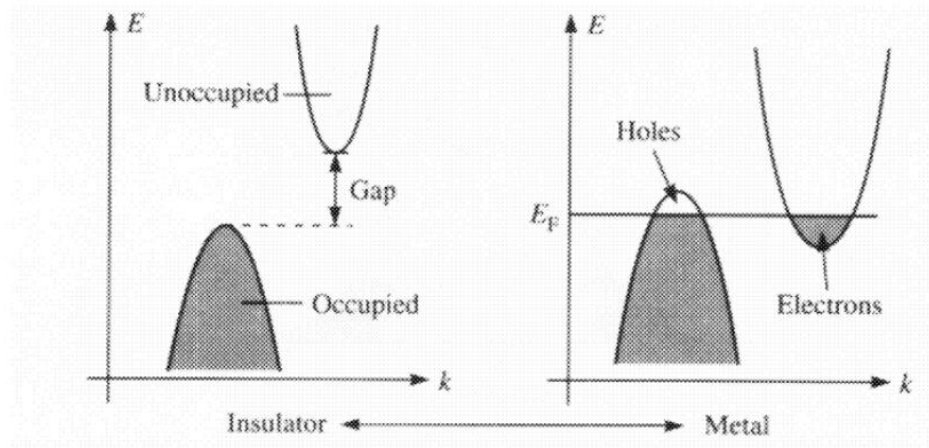


Figure 2.7: The interchange between insulator and metal [39].

2.6.11 Density of states

Total Density of states provide the number of all electrons allowed to occupy in given energy level. It is mathematically expressed as the following expression

$$\rho(\varepsilon) = \sum_n \langle \Psi_n | \Psi_n \rangle \delta(\varepsilon - \varepsilon_n) \quad (2.105)$$

Total density of states can be written as the sum of all projected density of states.

$$\rho(\varepsilon) = \sum_i \rho_i(\varepsilon) \quad (2.106)$$

Where $\rho_i(\varepsilon)$ is the projected density of states used to project each atomic orbital out and by using

$1 = \sum_i |i\rangle \langle i|$, we can introduce

$$\rho_i(\varepsilon) = \sum_n \langle \Psi_n | i \rangle \langle i | \Psi_n \rangle \delta(\varepsilon - \varepsilon_n) \quad (2.107)$$

3.CALCULATION DETAILS

In this work, the ground state energy of MgF_2 and CaF_2 were theoretically calculated via Cambridge Serial Total Energy Package (CASTEP) [40]. The GGA was chosen as a correlation functional and ultrasoft pseudopotentials was chosen as a pseudopotential for the DFT calculation. The results are used to calculate the electronic band structures at various pressure. Due to the decreasing of Bandgap of CaF_2 at 70 GPa, we introduced Mg to host materials, CaF_2 . To find the most thermodynamically stable of Mg doped CaF_2 , the lowest formation enthalpy of the mixture was determined by Alloy-Theoretic-Automated Toolkit (ATAT). After we find the concentration of Mg that minimized the energy of $\text{Mg}_{0.25}\text{Ca}_{0.75}\text{F}_2$, we then use the mixture as a input structure in CASTEP and calculate the band structure above 70 GPa and the density of states at 70 GPa. The workflow of this work is shown in Figure 3.1.

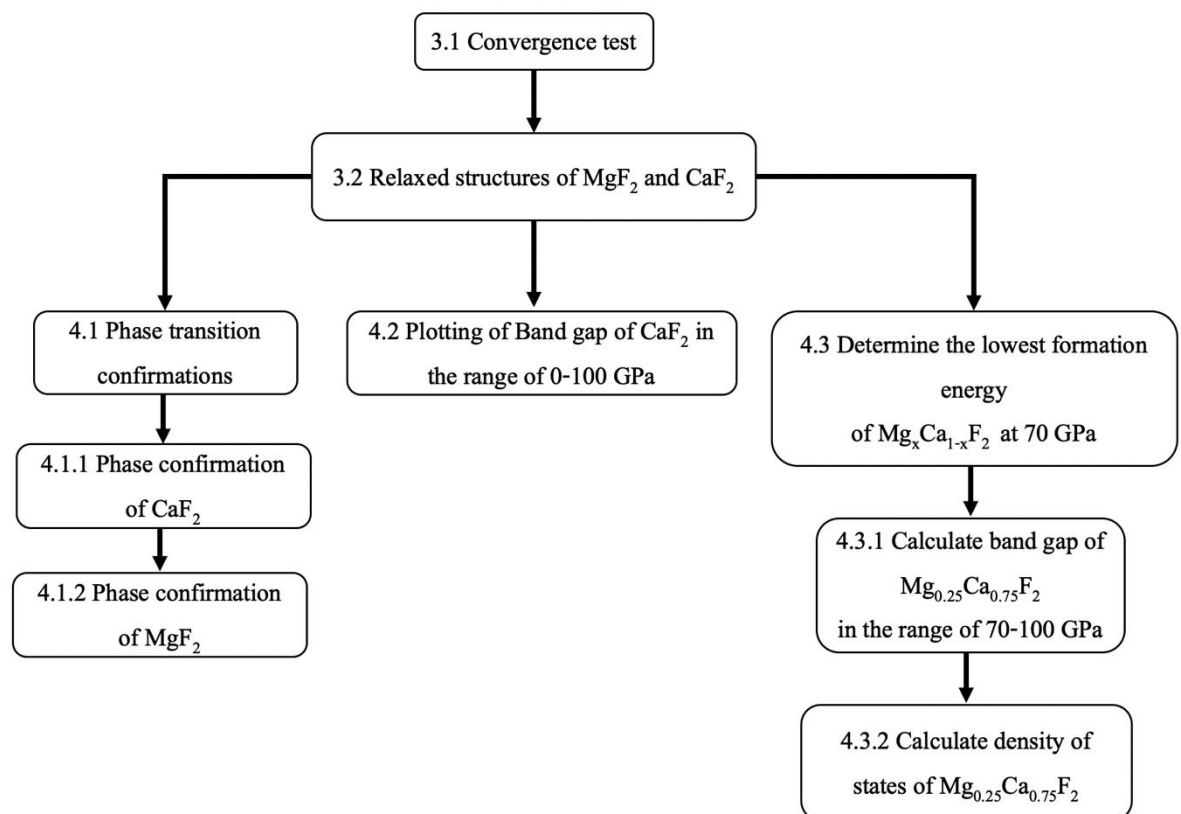


Figure 3.1: Workflow for computational calculations.

3.1 Convergence test of CaF₂

The convergence tests are necessary to determine the accuracy of total ground-state energy of the system. The parameters needed to be varied are the kinetic cutoff energies and the k-point grid. We optimised the face-centered cubic structure of CaF₂. After the atoms in the unit cell were relaxed. There are two graphs of convergence test of CaF₂ needed to be plotted. First, we choose the k-point grid of 0.04 Å⁻¹ and treated it as a fixed parameter, then we started varying the kinetic cutoff energies from 250 to 600 eV. Now we plotted the relation of total energies, as shown in Figure 3.2, with respect to y-axis and the kinetic cutoff energy with respect to x-axis. We see that the energy rapidly decreases from -2330.0 to -2332.3 eV then it slowly decreases from -2332.8 to -2.333.0 eV and converges to -2333.0 eV. Therefore, we selected 500 eV as cutoff energy. Moreover, we can select both of 450 and 550 eV because the total energy of these two values are nearly the same and the difference of energies in the range of 450 to 550 is nearly zero. Since other values give no difference in evaluating total energy of this system.

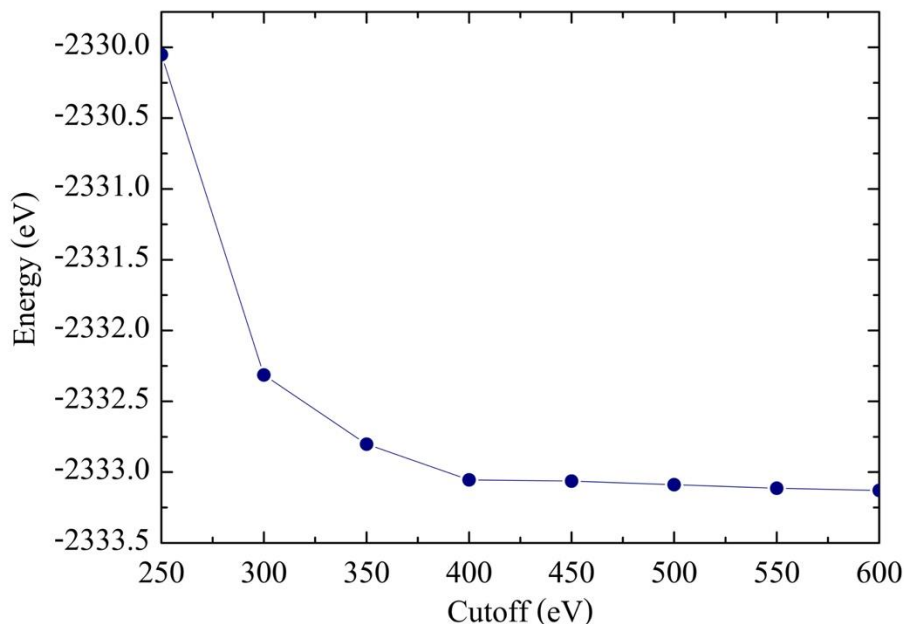


Figure 3.2: The relation between energy and the cutoff energy

For the Second graph, we choose the cutoff energy of 500 eV and treated it as a fixed parameter, then we started varying the k-point grid from 0.09 to 0.02 \AA^{-1} . Now we plotted the relation of calculated total energies with respect to y-axis and the k-point grid with respect to x-axis, see Figure 3.3. We see the difference of energies between k-point grid of 0.04 and 0.02 \AA^{-1} is in order of 10^{-5} eV which is very small. Therefore, we can choose k-point grid in the range of 0.04-0.02 \AA^{-1} . We used k-point grid of 0.04 \AA^{-1} and the cutoff energy of 500 eV as an input for further calculations.

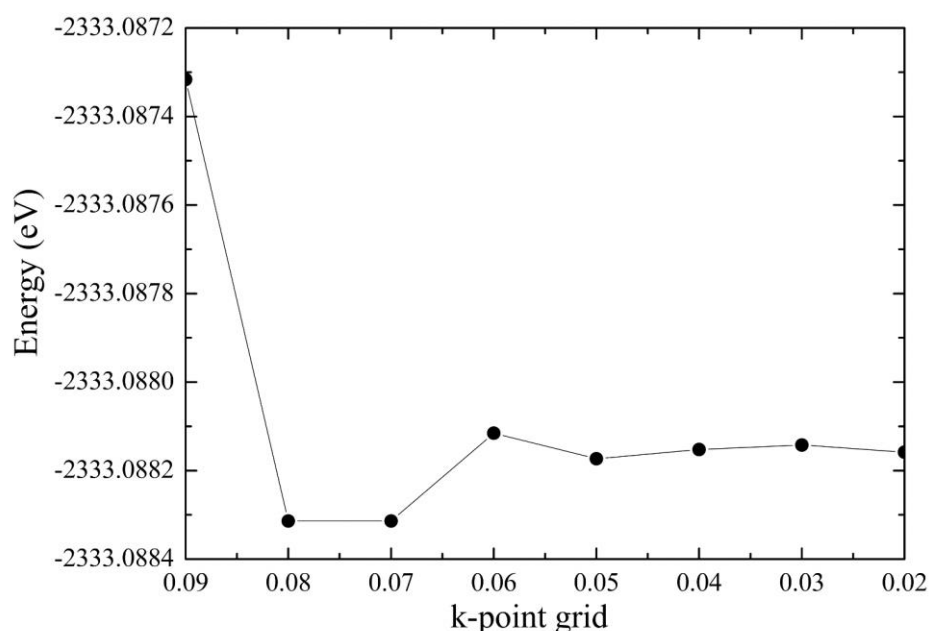


Figure 3.3: The relation between energy and the k-point grid if cutoff is fixed at 500 eV

3.2 Relaxed structures of CaF_2 and MgF_2

In this work, the structures with the cutoff energy of 500 eV k-point grid of 0.04 \AA^{-1} , which mentioned in the previous section, are defined as the relaxed structure. The relaxed atomic positions and the pictures of CaF_2 , MgF_2 are shown in Table 1-2, and in Figure 3.4. The relaxed structures will be used as an input for cluster expansion, band structure calculation, and density of states calculation.

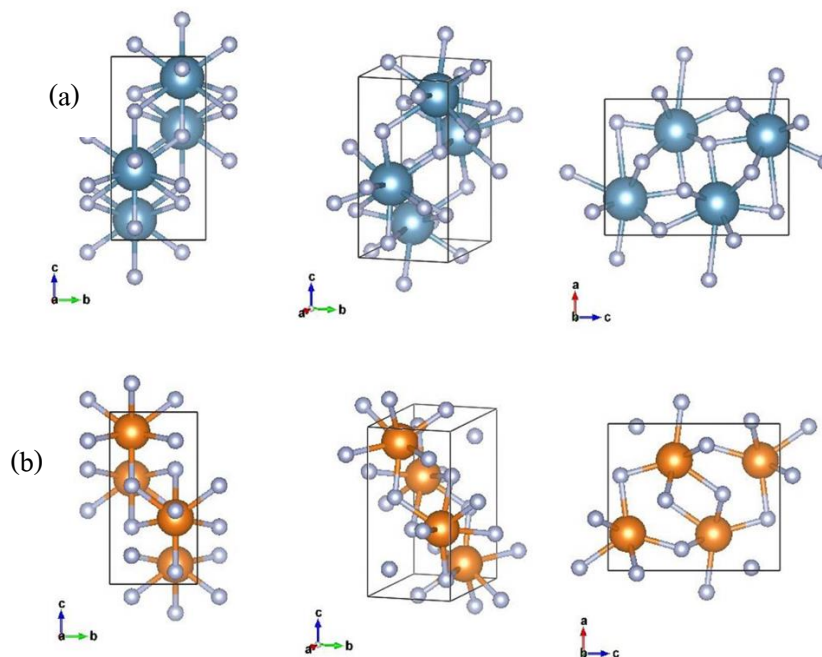


Figure 3.4: (a) relaxed CaF_2 at 70 GPa and (b) relaxed MgF_2 at 70 GPa [41]

Table 1: Atomic fractional coordinates of relaxed CaF_2

Lattice parameters			angles		
a	b	c	α	β	γ
4.79190	3.34040	6.47670	90.0000	90.0000	90.0000

Atoms	Structure parameters		
	x	y	z
Ca0	0.23242	0.75000	0.61261
F1	0.03805	0.75000	0.29864
F2	0.17162	0.75000	0.93307

Table 2: Atomic fractional coordinates of relaxed MgF_2

Lattice parameters			angles		
a	b	c	α	β	γ
4.96000	2.93210	5.84680	90.0000	90.0000	90.0000

Atoms	Structure parameters		
	x	y	z
Mg0	-0.25198	0.25000	-0.11814
F1	-1.02152	0.25000	0.16791
F2	-0.64743	0.25000	0.92895

4.RESULTS AND DISCUSSIONS

4.1 Phase transitions confirmation

4.1.1 Phase confirmation of CaF_2

We plot the enthalpy difference between the $\text{Fm}\bar{3}\text{m}$ and Pnma phases of CaF_2 versus pressure to confirm the phase transition of CaF_2 , as shown in Figure 4.1. We set the enthalpies of the Pnma phase at various pressures as a reference therefore the enthalpy difference of Pnma is zero along the pressure range, as depicted by black dots. Our calculations are also agreeable with Cui et al. Hence, CaF_2 adopts Fm-3m structure in the range of 0-8 GPa and Pnma above 8 GPa.

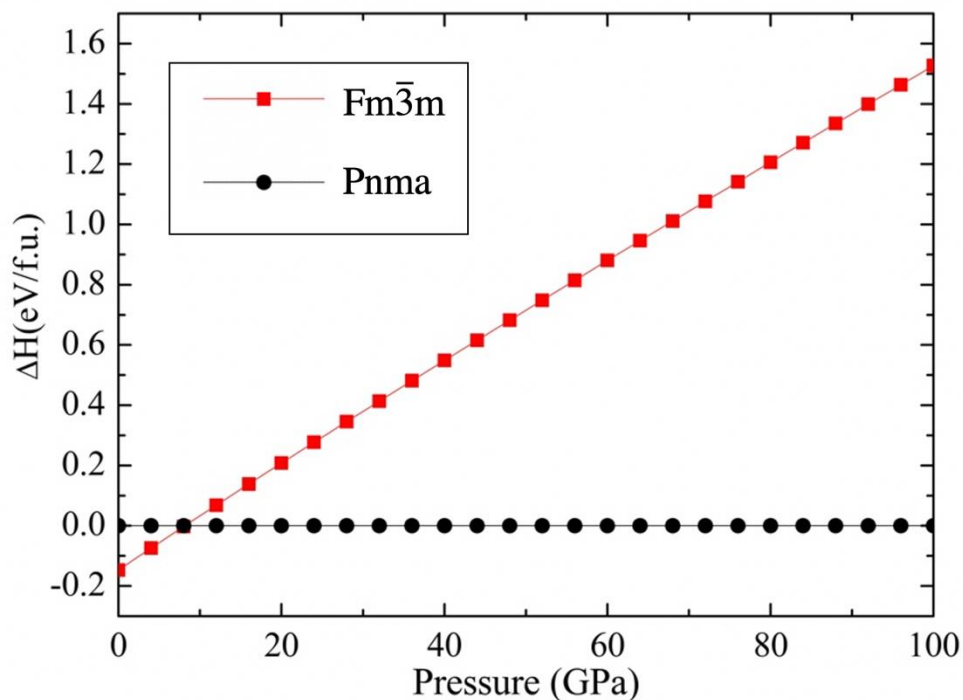


Figure 4.1: The enthalpy difference between the $\text{Fm}\bar{3}\text{m}$ and Pnma phases of CaF_2 as a function of pressure (red squares) [41].

In 2006, Wu *et al.* [13] have predicted that the phase of CaF_2 is P63/mmc above 70 GPa but our phonon dispersion relations of CaF_2 at 80 GPa and 100 GPa indicate that the Pnma phase is stable since there is no imaginary frequency so the equilibrium positions of CaF_2 are the same, see Figure 4.2 and 4.3. Therefore, the phase of CaF_2 should be Pnma above 70 GPa.

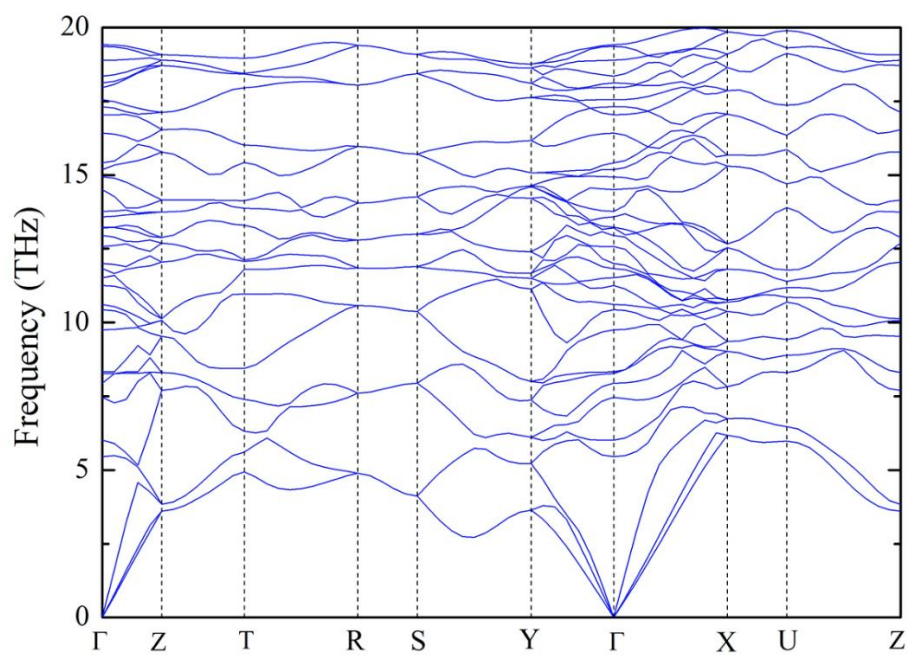


Figure 4.2: Phonon dispersion relation of Pnma phases of CaF₂ at 80 GPa.

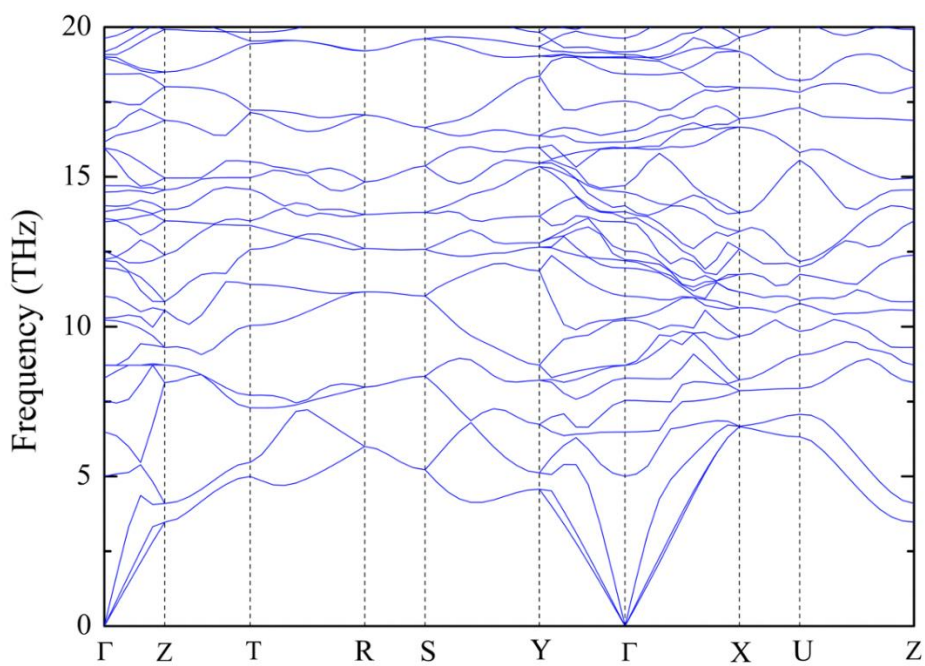


Figure 4.3: Phonon dispersion relation of Pnma phases of CaF₂ at 100 GPa

4.1.2 Phase confirmation of MgF₂

In 2017, Nelson J R., et al.[8] have predicted that the phase of MgF₂ is Pnma at 70 GPa. Our phonon dispersion relation of MgF₂ at 70 GPa is consistent with their work because the Pnma phase is stable at this pressure, see Figure 4.4. Due to the stability of CaF₂ and MgF₂ at 70 GPa, we can perform cluster expansion of Mg_xCa_{1-x}F₂ at 70 GPa.

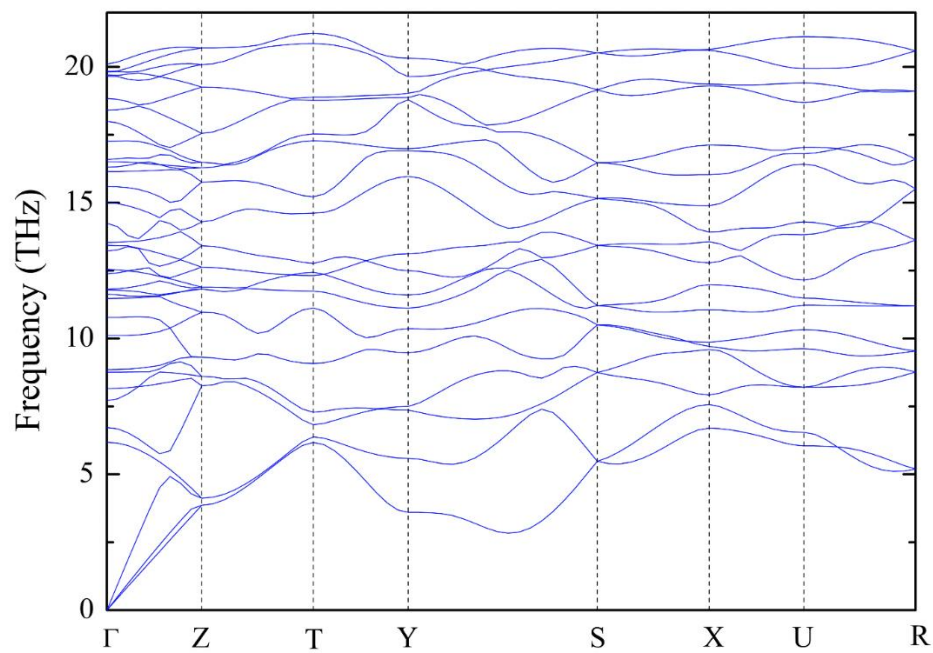


Figure 4.4: Phonon dispersion relation of Pnma phases of MgF₂ at 70 GPa

4.2 Plotting of bandgap of CaF_2 versus pressure

In this section, we investigate the pressure at which the bandgap of CaF_2 collapses. The bandgap as a function of pressure of the $\text{Fm}\bar{3}\text{m}$ and Pnma phases of CaF_2 is shown in Fig 4.5. We found that CaF_2 is a wide-bandgap insulator under pressure, and the bandgap increases in the range of 0 - 70 GPa, but slightly collapses between 70-100 GPa. This is in good agreement with the theoretical results of Wu *et al.* [13].

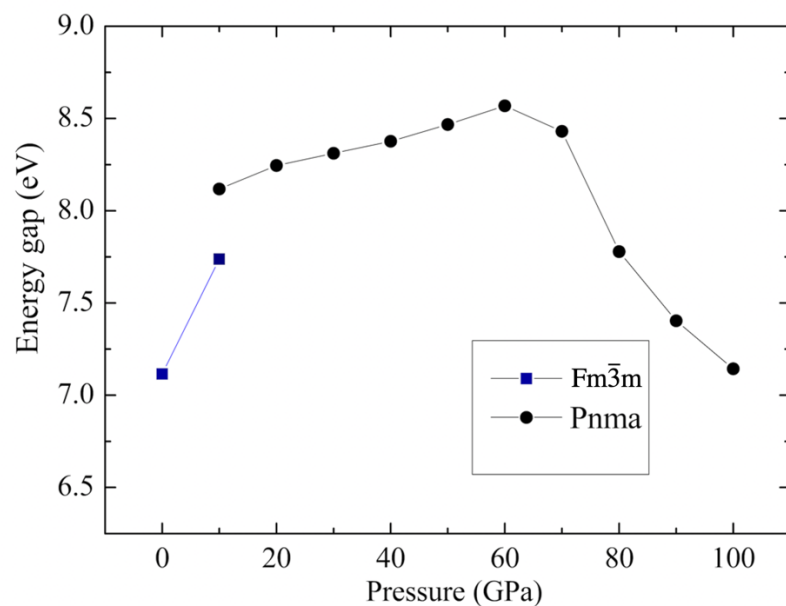


Figure 4.5: The bandgap versus pressure where blue squares represent energy gap of $\text{Fm}\bar{3}\text{m}\text{-CaF}_2$ and black circles represent energy gap of $\text{Pnma}\text{-CaF}_2$ [41].

4.3 Determining the lowest formation energy of $\text{Mg}_x\text{Ca}_{1-x}\text{F}_2$ at 70 GPa

The atomic positions from section 3.2 were used as input structures for cluster expansion technique. In Figure 4.6, ATAT [42] several structures with various atomic arrangements and compositions then the energy of each structure is determined by cluster expansion.

These energies are called “known structures” (known str), depicted as black dot. This step saves a lot of time and computational cost because cluster expansion provides us a glimpse on how the structure with low energy would be and it would be a time consuming process if we use DFT to calculate energy alone without knowing a structure from cluster expansion. Now, the first principle calculations are used to recalculate the energy from each red dot. If the energy from the cluster expansion is equal to the energy from first principle calculations, we obtain the “Predicted” structures (blue square dots). After the structure searching is completely conducted, the lowest energy from red triangle is called “known ground state (known gs)”. The formation energy can be used to compare the energy obtained from DFT written as [43]

$$H[\text{Mg}_x\text{Ca}_{1-x}] = E[\text{Mg}_x\text{Ca}_{1-x}] - (1-x)E[\text{Ca}] + xE[\text{Mg}] \quad (2.109)$$

Where x is concentration of Mg, $E[\text{Mg}_x\text{Ca}_{1-x}]$ is the free energy of $\text{Mg}_x\text{Ca}_{1-x}$, $E[\text{Ca}]$ and $E[\text{Mg}]$ are the free energies of Ca and Mg, respectively.

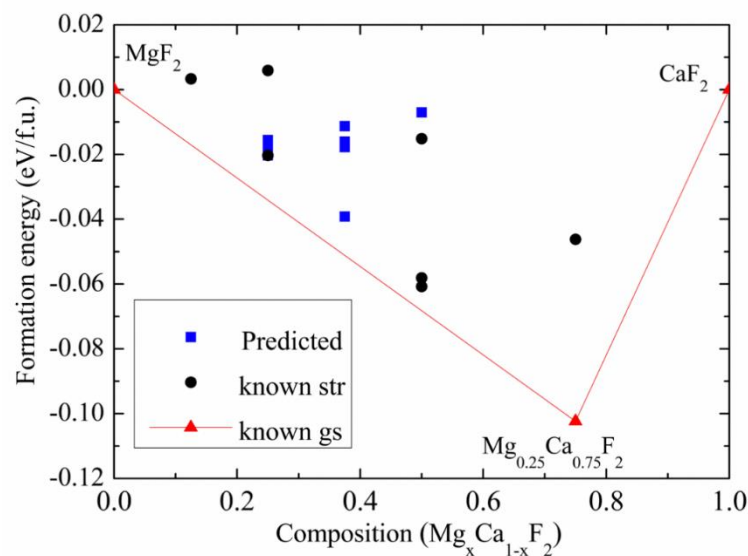


Figure 4.6: A plot of energy with the varying elemental composition of $\text{Mg}_x\text{Ca}_{1-x}\text{F}_2$ at 70 GPa, where “known str” indicates the energy obtained from relaxed structures evaluated by DFT (black dots), “Predicted” denotes the energy of the corresponding structures predicted from cluster expansion (blue square dots), and finally “known gs” accounts for the minimum energy

confirmed by DFT (red triangle dot). The convex hull depicted shows that $\text{Mg}_{0.25}\text{Ca}_{0.75}\text{F}_2$ has lowest energy [41].

The ATAT result shows that the most stable composition at 70 GPa is $\text{Mg}_{0.25}\text{Ca}_{0.75}\text{F}_2$ with a Pm structure. The atomic positions obtained from ATAT were then optimized in CASTEP. The optimized Pm structure of $\text{Mg}_{0.25}\text{Ca}_{0.75}\text{F}_2$ is shown in figure Figure 4.7. The lattice parameters, as shown in Table 3, at this pressure are $a = 6.2393$, $b = 3.1530$, and $c = 5.1317$, where $\alpha = \gamma = 90^\circ$, and $\beta = 91.3989$. Then, we continued by using this structure as an input for band structure and density of states calculation via CASTEP.

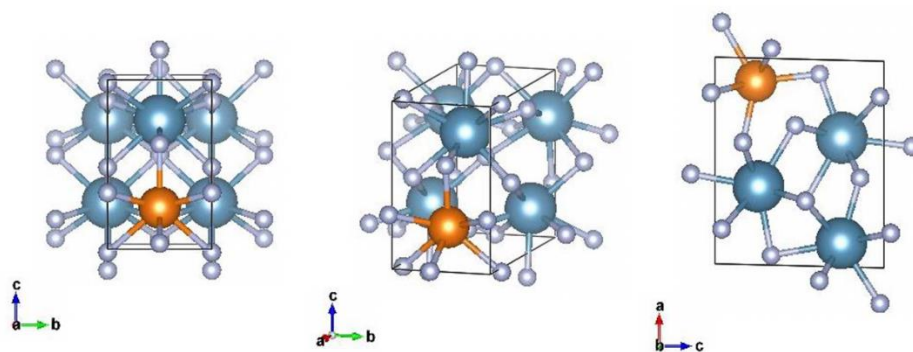


Figure 4.7: The relation between energy and the k-point grid if cutoff is fixed at 500 eV [41]

Table 3: Atomic fractional coordinates of relaxed $\text{Mg}_{0.25}\text{Ca}_{0.75}\text{F}_2$ at 70 GPa

Lattice parameters			angles		
a	b	c	α	β	γ
6.23930	3.15300	5.13170	90.0000	91.3989	90.0000

Atoms	Structure parameters		
	x	y	z
Ca1	0.62556	0.50000	0.75143
Mg1	0.88856	0.50000	0.24238
F2	0.16891	0.50000	0.03996
F3	0.31464	0.50000	0.53518
F6	0.59108	0.50000	0.16495
F7	0.93045	0.50000	0.61836
Ca2	0.37833	0.00000	0.25715
Ca3	0.11522	0.00000	0.74748
F1	0.82702	0.00000	0.97612
F4	0.67905	0.00000	0.47501
F8	0.43207	0.00000	0.85807
F5	0.04811	0.00000	0.33391

4.3.1 Electronic band structures of $\text{Mg}_x\text{Ca}_{1-x}\text{F}_2$, MgF_2 and CaF_2 at 70 GPa

From the electronic band structure of relaxed CaF_2 , as depicted in Figure 4.8, at 70 GPa, we see that it is an insulator because of a large forbidden gap, 8.430 eV, between the conduction band and valence band. The gap between conduction band and valence band of MgF_2 is 9.608 eV which is wider than that of CaF_2 , see Figure 4.9. With the introduction of Mg to the system of CaF_2 , $\text{Mg}_{0.25}\text{Ca}_{0.75}\text{F}_2$ is still an insulator at 70 GPa since the bandgap of $\text{Mg}_{0.25}\text{Ca}_{0.75}\text{F}_2$ is 8.626 eV, see Figure 4.10 and Table 4. The electrons fully occupy the valence state so it takes a tremendous amount of energy to take the electron from valence band to conduction band.

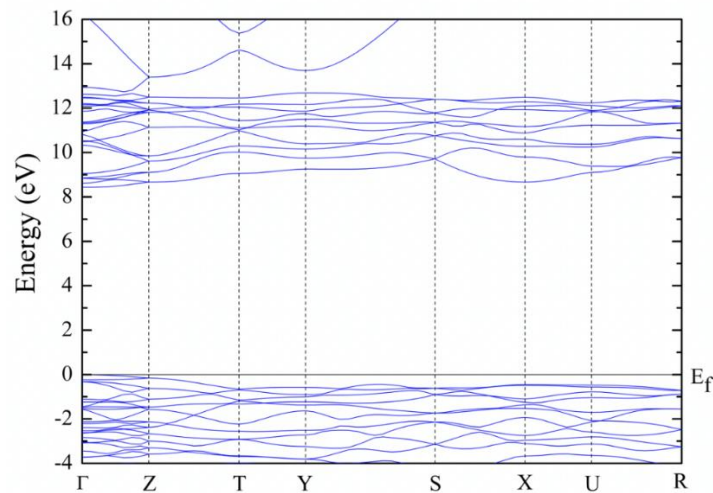


Figure 4.8: The electronic band structure of the relaxed CaF_2 at 70 GPa.

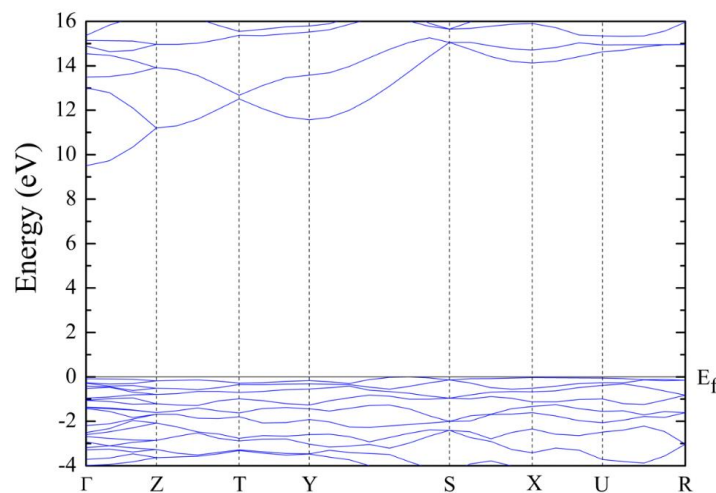


Figure 4.9: The electronic band structure of the relaxed MgF_2 at 70 GPa.

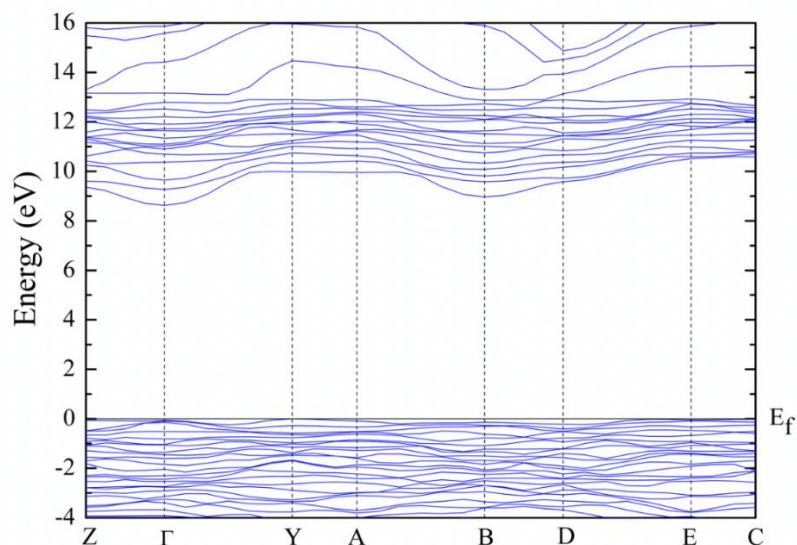


Figure 4.10: The electronic band structure of the relaxed $\text{Mg}_{0.25}\text{Ca}_{0.75}\text{F}_2$ at 70 GPa.

The bandgap as a function of pressure of $\text{Mg}_{0.25}\text{Ca}_{0.75}\text{F}_2$ is also shown in Figure 4.11 and in Table 4, compared with that of CaF_2 . It is also a wide-bandgap insulator under pressure, but the bandgap is slightly less than that of CaF_2 at pressure less than 70 GPa. The bandgap of $\text{Mg}_{0.25}\text{Ca}_{0.75}\text{F}_2$ increases as pressure increases, and is greater than that of CaF_2 in the pressure range of 70-100 GPa.

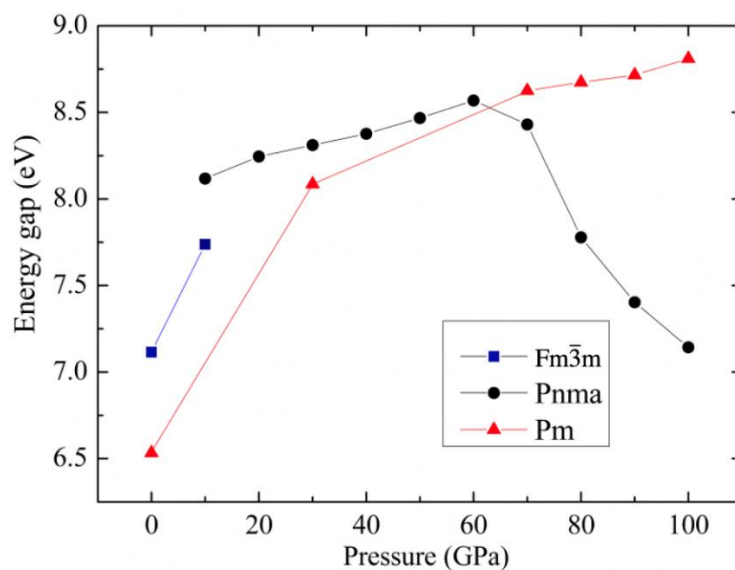


Figure 4.11: The bandgap versus pressure where black squares and red circles represent energy gap of CaF_2 and blue triangles represent energy gap of $\text{Mg}_{0.25}\text{Ca}_{0.75}\text{F}_2$ [41].

Table 4: The bandgap of CaF_2 and $\text{Mg}_{0.25}\text{Ca}_{0.75}\text{F}_2$

Pressure (Gpa)	Energy gap of CaF_2 (eV)		Energy gap of $\text{Mg}_{0.25}\text{Ca}_{0.75}\text{F}_2$ (eV)
	Fm-3m	Pnma	Pm
0	7.115	-	6.533
10	7.738	8.118	-
20	-	8.245	-
30	-	8.311	8.086
40	-	8.376	-
50	-	8.476	-
60	-	8.569	-
70	-	8.430	8.626
80	-	7.778	8.674
90	-	7.403	8.716
100	-	7.143	8.810

4.3.2 Projected density of states of $\text{Mg}_x\text{Ca}_{1-x}\text{F}_2$, MgF_2 and CaF_2

From the projected density of states of $\text{Mg}_{0.25}\text{Ca}_{0.75}\text{F}_2$ at 0 GPa, the p-band of F dominates the valence band maximum (VBM), whereas the s-band of Mg and Ca dominate the conduction band minimum (CBM), as shown in Figure 4.12. At 70 GPa, the p-band of F still dominates the VBM, but the s-band and p-band of Mg dominate the CBM, as shown in Figure 4.13.

Furthermore, the projected density of states of CaF_2 at 70 GPa, the p-band of F dominates the conduction band maximum (CBM), see Figure 4.14. If we compare the CBM of CaF_2 at 70 GPa with the CBM of MgF_2 , see Figure 4.15, and $\text{Mg}_{0.25}\text{Ca}_{0.75}\text{F}_2$ at 70 GPa, we see that the CBM of MgF_2 and $\text{Mg}_{0.25}\text{Ca}_{0.75}\text{F}_2$ at 70 GPa are dominated by s-band and p-band of Mg.

Finally, our PDOS calculations show that the electronic states of Mg dictate the bandgap behavior at this pressure. Therefore, Ca/Mg-substitution technique prevents the collapsing bandgap of CaF_2 .



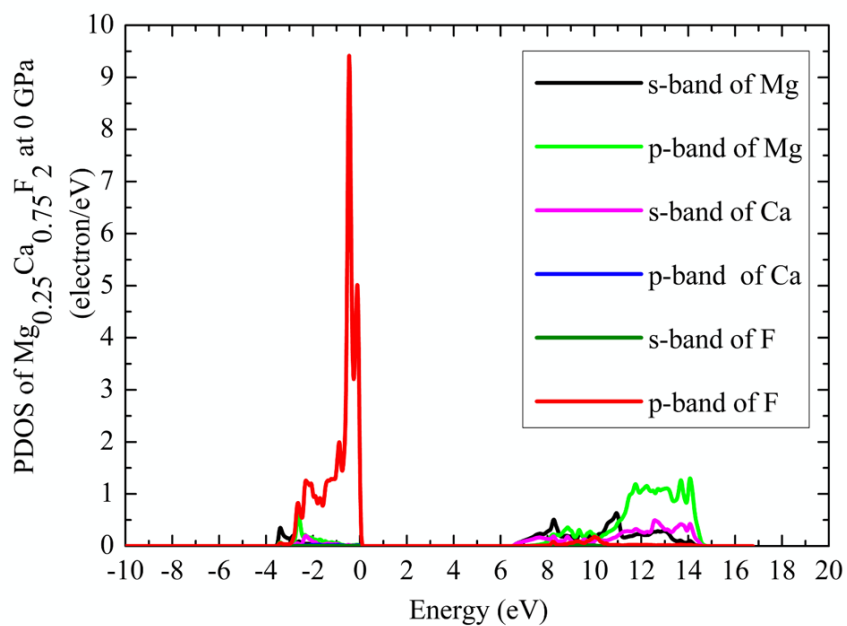


Figure 4.12: The projected density of the $\text{Mg}_{0.25}\text{Ca}_{0.75}\text{F}_2$ at 0 GPa [41]

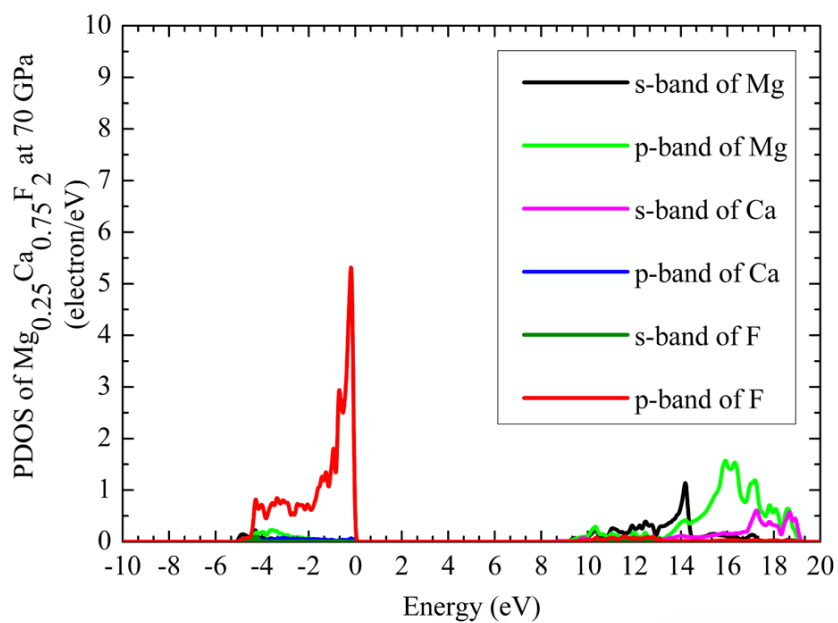
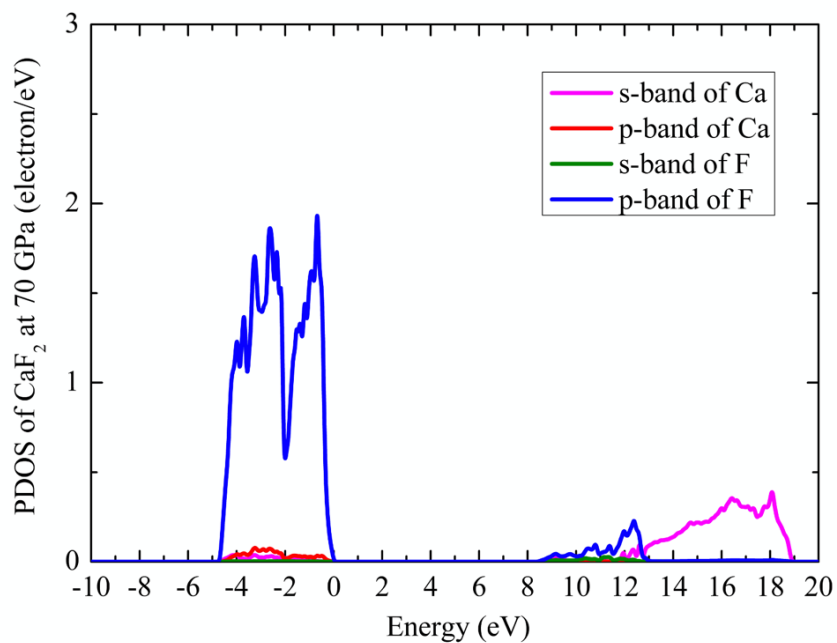
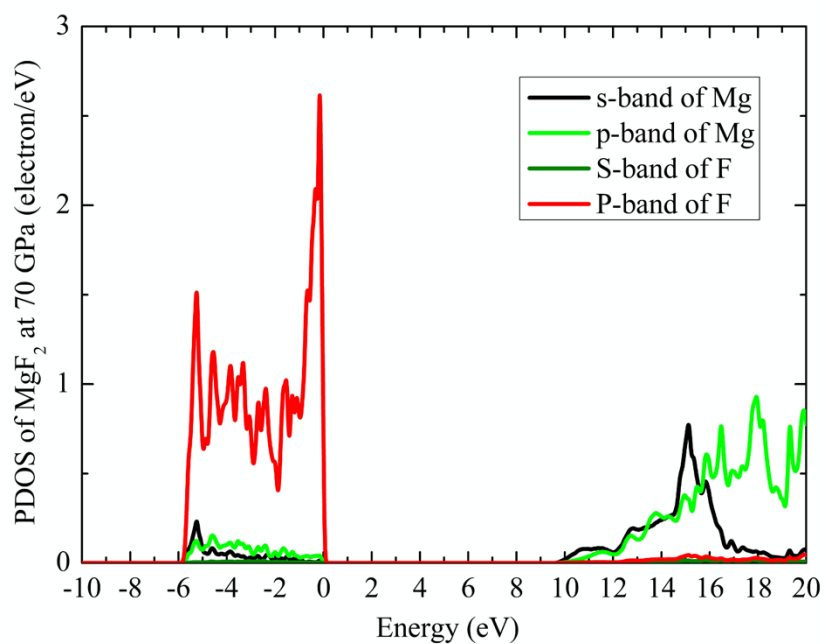


Figure 4.13: The projected density of the $\text{Mg}_{0.25}\text{Ca}_{0.75}\text{F}_2$ at 70 GPa [41]

Figure 4.14: The projected density of the CaF₂ at 70 GPaFigure 4.15: The projected density of the MgF₂ at 70 GPa

5. CONCLUSION

We deployed the cluster expansion technique to search the thermodynamically stable structure of $\text{Mg}_x\text{Ca}_{1-x}\text{F}_2$, which turns out to be $\text{Mg}_{0.25}\text{Ca}_{0.75}\text{F}_2$ with Pm structure. We then used this structure to calculate the band structure and the projected density of states in various ranges of pressure. Our results indicate that the electronic states of Mg dominate the CBM at around 70 GPa. Hence, the bandgap of $\text{Mg}_{0.25}\text{Ca}_{0.75}\text{F}_2$ beyond 70 GPa is governed by the electronic states of Mg. In other words, the Ca/Mg-substitution technique prevents the bandgap of this fluoride compound from collapsing from 70 GPa onwards. Furthermore, we suggest that our Ca/Mg-substituted fluoride can be used as an internal pressure calibrator since the plot between the bandgap and pressure is almost a linear relationship.



REFERENCES

- [1] Wan Y, Xiong G, Luo H, He F, Huang Y and Zhou X 2008 Preparation and characterization of a new biomedical magnesium–calcium alloy *Materials & Design* **29** 2034-7
- [2] Song J, Wang Z, Huang Y, Srinivasan A, Beckmann F, Kainer K U and Hort N 2015 Hot tearing susceptibility of Mg-Ca binary alloys *Metallurgical and Materials Transactions A* **46** 6003-17
- [3] Zeng R-C, Qi W-C, Cui H-Z, Zhang F, Li S-Q and Han E-H 2015 In vitro corrosion of as-extruded Mg–Ca alloys—the influence of Ca concentration *Corrosion Science* **96** 23-31
- [4] Song M-S, Zeng R-C, Ding Y-F, Li R W, Easton M, Cole I, Birbilis N and Chen X-B 2019 Recent advances in biodegradation controls over Mg alloys for bone fracture management: a review *Journal of materials science & technology* **35** 535-44
- [5] Deng M, Höche D, Lamaka S V, Snihirova D and Zheludkevich M L 2018 Mg-Ca binary alloys as anodes for primary Mg-air batteries *Journal of Power Sources* **396** 109-18
- [6] Liu F, Wang T, Liu X and Fan L Z 2020 Challenges and Recent Progress on Key Materials for Rechargeable Magnesium Batteries *Advanced Energy Materials* 2000787
- [7] Cui S, Feng W, Hu H, Feng Z and Wang Y J C m s 2009 Structural stabilities, electronic and optical properties of CaF₂ under high pressure: A first-principles study **47** 41-5
- [8] Nelson J R, Needs R J and Pickard C J 2017 High-pressure phases of group-II difluorides: Polymorphism and superionicity *Physical Review B* **95** 054118
- [9] Dorfman S M, Jiang F, Mao Z, Kubo A, Meng Y, Prakapenka V B and Duffy T S J P R B 2010 Phase transitions and equations of state of alkaline earth fluorides CaF₂, SrF₂, and BaF₂ to Mbar pressures **81** 174121
- [10] Daimon M and Masumura A J A o 2002 High-accuracy measurements of the refractive index and its temperature coefficient of calcium fluoride in a wide wavelength range from 138 to 2326 nm **41** 5275-81
- [11] Qiu W, Ma Z, Patel D, Sang L, Cai C, Shahriar Al Hossain M, Cheng Z, Wang X, Dou S X J A a m and interfaces 2017 The interface structure of FeSe thin film on CaF₂ substrate and its influence on the superconducting performance **9** 37446-53

- [12] Hazen R and Finger L J J o A C 1981 Calcium fluoride as an internal pressure standard in high-pressure crystallography **14** 234-6
- [13] Wu X, Qin S and Wu Z J P R B 2006 First-principles study of structural stabilities, and electronic and optical properties of Ca F₂ under high pressure **73** 134103
- [14] Balaji T, Lifante G, Daran E, Legros R and Lacoste G J T S F 1999 Growth by molecular beam epitaxy and characterization of CaF₂: Pr³⁺ planar waveguides **339** 187-93
- [15] Khiari S, Velázquez M, Moncorgé R, Doualan J-L, Camy P, Ferrier A, Diaf M J J o a and compounds 2008 Red-luminescence analysis of Pr³⁺ doped fluoride crystals **451** 128-31
- [16] Wang Q, Su L, Li H, Zheng L, Guo X, Jiang D, Zhao H, Xu J, Ryba-Romanowski W, Solarz P J J o a and compounds 2011 Optical spectra and excited state relaxation dynamics of Nd³⁺ in CaF₂ single crystal **509** 8880-4
- [17] Sharonov M Y, Bratus A, Sevastyanov B, Zhmurova Z, Bystrova A, Krivandina E, Demianets L and Sobolev B J O c 1994 The amplification and excited state absorption of Nd-doped nonstoichiometric crystals with fluorite structure in the 1.3 μm region **111** 245-52
- [18] Qi Y-Y, Li Z-G, Cheng Y, Chen X-R and Ji G-F J Z f N A 2015 First-principles study of electronic, elastic, and optical properties of Yb: CaF₂ crystals **70** 889-96
- [19] Dakui D and Fuding M 1994 Glass formation and crystallization in AlF₃ YF₃ BaF₂ CaF₂ MgF₂ *Journal of non-crystalline solids* **168** 275-80
- [20] Elliott D L 2014 *Ultraviolet laser technology and applications*: Academic press)
- [21] Sukmas W, Pinsook U, Tsuppayakorn-aeek P, Pakornchote T, Sukserm A and Bovornratanaraks T 2019 Organic Molecule Orientations and Rashba—Dresselhaus Effect in α-Formamidinium Lead Iodide *The Journal of Physical Chemistry C* **123** 16508-15
- [22] Born M and Oppenheimer J R 1927 On the quantum theory of molecules *Сборник статей к мультимедийному электронному учебно-методическому комплексу по дисциплине «физика атома и атомных явлений» отв. ред. Шундалов МБ: БГУ. Физический факультет*
- [23] Fock V 1930 Näherungsmethode zur Lösung des quantenmechanischen Mehrkörperproblems *Zeitschrift für Physik* **61** 126-48
- [24] Hohenberg P and Kohn W 1964 Inhomogeneous electron gas *physical review* **136** B864
- [25] Koch W and Holthausen M C 2015 *A chemist's guide to density functional theory*: John Wiley & Sons)

- [26] Ceperley D M and Alder B J 1980 Ground state of the electron gas by a stochastic method *Physical Review Letters* **45** 566
- [27] Perdew J P, Burke K and Ernzerhof M 1996 Generalized gradient approximation made simple *Physical review letters* **77** 3865
- [28] Bloch F 1929 Über die quantenmechanik der elektronen in kristallgittern *Zeitschrift für physik* **52** 555-600
- [29] Blöchl P E 1994 Projector augmented-wave method *Physical review B* **50** 17953
- [30] Baumeister P F 2013 *Real-Space Finite-Difference PAW Method for Large-Scale Applications on Massively Parallel Computers* vol 53: Forschungszentrum Jülich)
- [31] Phillips J C and Kleinman L 1959 New method for calculating wave functions in crystals and molecules *Physical Review* **116** 287
- [32] Vanderbilt D 1990 Soft self-consistent pseudopotentials in a generalized eigenvalue formalism *Physical review B* **41** 7892
- [33] Pfrommer B G, Côté M, Louie S G and Cohen M L 1997 Relaxation of crystals with the quasi-Newton method *Journal of Computational Physics* **131** 233-40
- [34] Head J D and Zerner M C 1985 A Broyden—Fletcher—Goldfarb—Shanno optimization procedure for molecular geometries *Chemical physics letters* **122** 264-70
- [35] Murnaghan F 1944 The compressibility of media under extreme pressures *Proceedings of the national academy of sciences of the United States of America* **30** 244
- [36] Birch F 1947 Finite elastic strain of cubic crystals *Physical review* **71** 809
- [37] Giustino F 2014 *Materials modelling using density functional theory: properties and predictions*: Oxford University Press)
- [38] Sharma A 1996 *Semiconductor Electronics*: New Age International)
- [39] Sutton A P 1993 *Electronic structure of materials*: Clarendon Press)
- [40] Clark S J, Segall M D, Pickard C J, Hasnip P J, Probert M I, Refson K and Payne M C J Z f K-C M 2005 First principles methods using CASTEP **220** 567-70
- [41] N Chintananon, P Tsuppayakorn-aek, W Sukmas, T Bovornratanaraks and U Pinsook 2020 Effects of Mg substitution on electronic properties of CaF₂ *Journal of Physics: Conference Series, Just Accepted Manuscript*
- [42] van de Walle A, Asta M and Ceder G 2002 The alloy theoretic automated toolkit: A user

guide *arXiv preprint cond-mat/0212159*

- [43] Alidoust M, Kleiven D and Akola J 2020 Density functional simulations of pressurized Mg-Zn and Al-Zn alloys *Physical Review Materials* **4** 045002





จุฬาลงกรณ์มหาวิทยาลัย
CHULALONGKORN UNIVERSITY

VITA

NAME Natthasart Chintananon

DATE OF BIRTH 4 May 1990

PLACE OF BIRTH Bangkok

INSTITUTIONS ATTENDED Chulalongkorn University

HOME ADDRESS 208/2 Moo 1 Chor. Rungrueng 6 Bangkruay-Sainoi Rd.
Bangrakpattana Bangbuathong Nonthaburi 11110

PUBLICATION Effects of magnesium substitution on electronic properties of calcium difluoride
Natthasart Chintananon, Prutthipong Tsuppayakorn-aeK,
Wiwittawin Sukmas, Thiti Bovornrattanakraks, and Udomsilp
Pinsook
Journal of Physics: Conference Series Just Accepted Manuscript